Remote Sensing of Environment 283 (2022) 113327

Contents lists available at ScienceDirect

Remote Sensing of Environment

journal homepage: www.elsevier.com/locate/rse

Seasonal dynamics of dissolved organic matter in the Mackenzie Delta, Canadian Arctic waters: Implications for ocean colour remote sensing

B. Juhls [a,b,c,*], A. Matsuoka [b,d], M. Lizotte [b], G. Bécu [b], P.P. Overduin [c], J. El Kassar [a], E. Devred [e], D. Doxaran [g], J. Ferland [b], M.H. Forget [b], A. Hilborn [e], M. Hieronymi [f], E. Leymarie [g], J. Maury [g], L. Oziel [b,h], L. Tisserand [i], D.O.J. Anikina [j], M. Dillon [k], M. Babin [b]

[a] Department of Geosciences, Institute of Meteorology, Freie Universität Berlin, Carl-Heinrich-Becker-Weg 6-10, 12165 Berlin, Germany
[b] Takuvik International Research Laboratory, Département de Biologie and Québec-Océan, Université Laval (Canada) & CNRS (France), Pavillon Alexandre-Vachon 1045, avenue de la Médecine, Local 2078, G1V 0A6, Canada
[c] Alfred Wegener Institute, Helmholtz Centre for Polar and Marine Research, Telegrafenberg A45, 14473 Potsdam, Germany
[d] Institute for the Study of Earth, Oceans, and Space, University of New Hampshire, Durham, NH 03824, USA
[e] Ocean and Ecosystem Sciences Division, Bedford Institute of Oceanography, Fisheries and Oceans Canada, 1 Challenger Dr, Dartmouth, NS B2Y 4A2, Canada
[f] Institute of Carbon Cycles, Helmholtz-Zentrum Hereon, Max-Planck-Straße 1, 21502 Geesthacht, Germany
[g] Laboratoire d'Océanographie de Villefranche (LOV), Sorbonne Université, CNRS, 181 Chemin du Lazaret, 06230 Villefranche-sur-Mer, France
[h] Alfred Wegener Institute, Helmholtz Centre for Polar and Marine Research, Am Handelshafen 12, 27570 Bremerhaven, Germany
[i] Laboratoire d'Océanographie Microbienne UMR7621 CNRS-Sorbonne Université, Observatoire Océanologique de Banyuls, Av. Pierre Fabre, 66650 Banyuls-sur-Mer, France
[j] Tuktoyaktuk Community Corporation, 274 Inuvialuit Lane, Tuktoyaktuk, NT X0E 1C0, Canada
[k] Inuvik Hunters and Trappers Committee, 107 MacKenzie Rd, Inuvik, NT X0E 0T0, Canada

ARTICLE INFO

Edited by Dr. Menghua Wang

Keywords:
Satellite ocean colour remote sensing
Dissolved organic matter
Mackenzie River
Beaufort Sea
Sentinel-3 OLCI
Land-ocean fluxes

ABSTRACT

Increasing air temperatures and associated permafrost thaw in Arctic river watersheds, such as the Mackenzie River catchment, are directly affecting the aquatic environment. As a consequence, the quantity and the quality of dissolved organic carbon (DOC) that is transported via the Mackenzie River into the Arctic Ocean is expected to change. Particularly in these remote permafrost regions of the Arctic, monitoring of terrigenous organic carbon fluxes is insufficient and knowledge of distribution and fate of organic carbon when released to the coastal waters is remarkably lacking. Despite its poorly evaluated performance in Arctic coastal waters, Satellite Ocean Colour Remote Sensing (SOCRS) remains a powerful tool to complement monitoring of land-ocean DOC fluxes, detect their trends, and help in understanding their propagation in the Arctic Ocean.

In this study, we use in situ and SOCRS data to show the strong seasonal dynamics of the Mackenzie River plume and the spatial distribution of associated terrigenous DOC on the Beaufort Sea Shelf for the first time. Using a dataset collected during an extensive field campaign in 2019, the performance of three commonly-used atmospheric correction (AC) algorithms and two available colored dissolved organic matter (CDOM) retrieval algorithms were evaluated using the Ocean and Land Colour Instrument (OLCI). Our results showed that in optically-complex Arctic coastal waters the Polymer AC algorithm performed the best. For the retrieval of CDOM, the gsmA algorithm (Mean Percentage Error (MPE) = 35.7%) showed slightly more consistent results compared to the ONNS algorithm (MPE = 37.9%). By merging our measurements with published datasets, the newly-established DOC-CDOM relationship for the Mackenzie-Beaufort Sea region allowed estimations of DOC concentrations from SOCRS across the entire fluvial-marine transition zone with an MPE of 20.5%. Finally, we applied SOCRS with data from the Sentinel-3 OLCI sensor to illustrate the seasonal variation of DOC concentrations in the surface waters of the Beaufort Sea on a large spatial scales and high frequency throughout the entire open water period. Highest DOC concentrations and largest lateral extent of the plume were observed in

* Corresponding author at: Alfred Wegener Institute, Helmholtz Centre for Polar and Marine Research, Telegrafenberg A45, 14473 Potsdam, Germany
E-mail addresses: bennet.juhls@awi.de (B. Juhls), atsushi.matsuoka@unh.edu (A. Matsuoka), martine.lizotte@arcticnet.ulaval.ca (M. Lizotte), guislain.becu@takuvik.ulaval.ca (G. Bécu), paul.overduin@awi.de (P.P. Overduin), jan.elkassar@met.fu-berlin.de (J. El Kassar), emmanuel.devred@dfo-mpo.gc.ca (E. Devred), david.doxaran@imev-mer.fr (D. Doxaran), joannie.ferland@environnement.gouv.qc.ca (J. Ferland), Marie-Helene.Forget@takuvik.ulaval.ca (M.H. Forget), andrea.hilborn@dfo-mpo.gc.ca (A. Hilborn), martin.hieronymi@hereon.de (M. Hieronymi), edouard.leymarie@imev-mer.fr (E. Leymarie), juliette.maury@obs-vlfr.fr (J. Maury), laurent.oziel@awi.de (L. Oziel), marcel.babin@takuvik.ulaval.ca (M. Babin).

https://doi.org/10.1016/j.rse.2022.113327
Received 22 April 2022; Received in revised form 30 September 2022; Accepted 18 October 2022
Available online 31 October 2022

spring right after the Mackenzie River ice break-up indicating that the freshet was the main driver of plume propagation and DOC distribution on the shelf. Satellite-derived images of surface water DOC concentration placed the in situ observations into a larger temporal and spatial context and revealed a strong seasonal variability in transport pathways of DOC in the Mackenzie- Beaufort Sea region.

1. Introduction

Warming in the Arctic watersheds is expected to affect the biogeochemistry of riverine and coastal waters (Frey and McClelland, 2009; Holmes et al., 2012a). Particularly, the mobilization of organic carbon from thawing permafrost (Frey and Smith, 2005) accompanied by an increase in river discharge (McClelland et al., 2006; Peterson, 2002) might have a significant impact not only on local carbon cycling but also on the global air-sea fluxes of carbon dioxide (CO_2) through physical and biogeochemical processes. Most of the terrestrial organic carbon is transported as dissolved organic carbon (DOC; mg L^{-1}) via rivers into the Arctic Ocean (McGuire et al., 2009). Arctic rivers are characterized by a strong seasonal variation of water discharge and, therefore, of DOC export to the Arctic Ocean (Holmes et al., 2012b; Juhls et al., 2020; Le Fouest et al., 2013; Raymond et al., 2007; Stedmon et al., 2011). This has essential implications regarding the distribution of DOC on Arctic shelves and complicates accurate monitoring.

The Mackenzie River is the fourth largest riverine freshwater source to the Arctic Ocean (Holmes et al., 2012b), releasing 1.17–1.66 Tg DOC yr^{-1} to the Beaufort Sea (Bertin et al., 2022). Almost half of its catchment area is underlain by continuous and discontinuous permafrost (Holmes et al., 2012b) and is thus especially vulnerable to warming in the Arctic (Frey and McClelland, 2009). Tank et al. (2016) reported a 39.3% increase in DOC flux from the Mackenzie River over the last four decades and suggested permafrost thaw as an important driver for this increase. While the monitoring of organic matter, associated carbon fluxes and their characteristics in Arctic rivers is steadily improving (Cooper et al., 2008; Holmes et al., 2012b; Juhls et al., 2020; Raymond et al., 2007; Stedmon et al., 2011; Tank et al., 2016), not much attention has been paid to the fluvial-marine transition zone, mostly due to the challenge it poses in terms of accessibility. These transition zones include estuarine, coastal, and near-shore waters, and are suspected to be crucial for the fate of organic carbon in the Arctic Ocean and in the overall cycling of carbon in the Arctic (Granskog et al., 2009; Lasareva et al., 2019; Vetrov et al., 2004). Several studies suggest that fluvial fluxes are substantially altered (e.g. by degradation and flocculation) in these transition zones before they reach the open Arctic Ocean (Emmerton et al., 2008; Holmes et al., 2012b; McClelland et al., 2012). However, distribution, transport pathways, and removal rates of terrigenous organic matter on the shelf are poorly constrained. Although several studies provided first insights into dissolved organic matter (DOM) fluxes and optical characteristics of the Mackenzie River (Mann et al., 2016; Raymond et al., 2007; Tank et al., 2016) and the offshore Beaufort Sea (Antoine et al., 2013; Doxaran et al., 2012; Fichot et al., 2013; Matsuoka et al., 2012, 2013), they focused on either the fluvial or marine system, leaving an understudied gap in the transition zone between them. The low number of samples across a large region and limited seasonal coverage collected in these coastal transition zones (Emmerton et al., 2008; Forest et al., 2014; Osburn et al., 2009; Retamal et al., 2008; Shen et al., 2012; Vallières et al., 2008) could not resolve the spatial distribution and seasonal patterns of the Mackenzie River plume and its changing optical DOM characteristics. A better understanding of the distribution of DOM including its quantity, quality, and related alteration processes is needed to understand the potential impact on future changes for the global carbon cycle.

Satellite Ocean Colour Remote Sensing (SOCRS) is a tool that facilitates the monitoring of surface water organic carbon concentration. The intensity of light absorption by colored dissolved organic matter ($a_{CDOM}(\lambda)$; m^{-1}) can be retrieved by satellite, for example empirically (Bélanger et al., 2008; Mannino et al., 2008), semi-analytically (Matsuoka et al., 2013), or via neural networks (e.g. Doerffer and Schiller, 2007; Hieronymi et al., 2017) and can be linked to DOC concentration through empirical relationships derived from in situ measurements (Massicotte et al., 2017; Matsuoka et al., 2013, 2017). The application of SOCRS to measure dissolved organic matter (DOM) concentrations and their distributions on large spatial scales in Arctic shelf waters is growing (Bertin et al., 2022; Fichot et al., 2013; Juhls et al., 2019; Matsuoka et al., 2016, 2017). SOCRS is a powerful tool, which provides synoptic views of water properties at high temporal resolution. On the other hand, SOCRS in Arctic coastal waters is challenged due to the presence of frequent cloud and ice cover, snow and sea-ice adjacency effects, low sun elevation and optically complex waters (Babin et al., 2015). Moreover, the performance of SOCRS in near-shore Arctic coastal waters is still poorly evaluated, mainly due to a lack of in situ observations.

To improve the use of SOCRS in Arctic shelf waters, Matsuoka et al. (2013) designed a new algorithm for the retrieval of $a_{CDOM}(443)$ using a semi-analytical approach, specifically adapted for Arctic waters. While the algorithm showed a reasonable accuracy (12% Mean Percentage Error(MPE)) in offshore waters of the Arctic Ocean (Matsuoka et al., 2017), the performance in optically complex near-shore waters has yet to be comprehensively evaluated. Recently, another CDOM retrieval algorithm, the OLCI Neural Network Swarm (ONNS), was designed by Hieronymi et al. (2017) for a broad range of water constituent concentrations. ONNS consists of several algorithms specialized for different optical water types including extremely highly absorbing and scattering near-shore waters. The evaluation of the ONNS algorithm was performed on the Laptev Sea shelf and included coastal waters near the Lena River mouth (Juhls et al., 2019). The ONNS algorithm showed reasonable agreement to in situ data ($r^2 = 0.72$) for the SOCRS retrieval of CDOM in these waters, which are comparable to the Beaufort Sea coastal waters.

Besides testing the accuracy of CDOM retrievals, the performance of the atmospheric correction algorithms in Arctic near-shore coastal waters also requires thorough evaluation, hence the requirement for in situ radiometric measurements. While recent studies by Mograne et al. (2019) and Renosh et al. (2020) investigated the performance of several atmospheric correction algorithms for Sentinel 3 OLCI in temperate waters, Arctic coastal waters remain largely understudied.

Another critical component needed to monitor DOC from space is a robust relationship between DOC concentration and CDOM absorption that is suited for the region of interest. Reported relationships from varying Arctic regions (Juhls et al., 2019; Mann et al., 2016; Matsuoka et al., 2017; Pugach et al., 2018) indicated that substantial regional and seasonal variability of DOM characteristics can affect these relationships. Matsuoka et al. (2012) established a relationship for the Beaufort Sea region which was, however, limited in its validity to summer months and mostly offshore waters. In order to provide accurate estimates of DOC concentrations across the fluvial-marine transition zone using SOCRS, CDOM-DOC relationships require inclusion of a wider range of water types across domains.

This study aims at improving the understanding of the seasonal and spatial variability of DOC in the fluvial-marine transition zone in the Mackenzie River – Beaufort Sea region using in situ and SOCRS data. We first evaluate the performance of multiple SOCRS algorithms and establish a new DOC-CDOM relationship to monitor DOC concentrations from space. Second, we employ SOCRS to display the seasonal variability of DOC distribution on the Beaufort Sea Shelf on a larger spatial

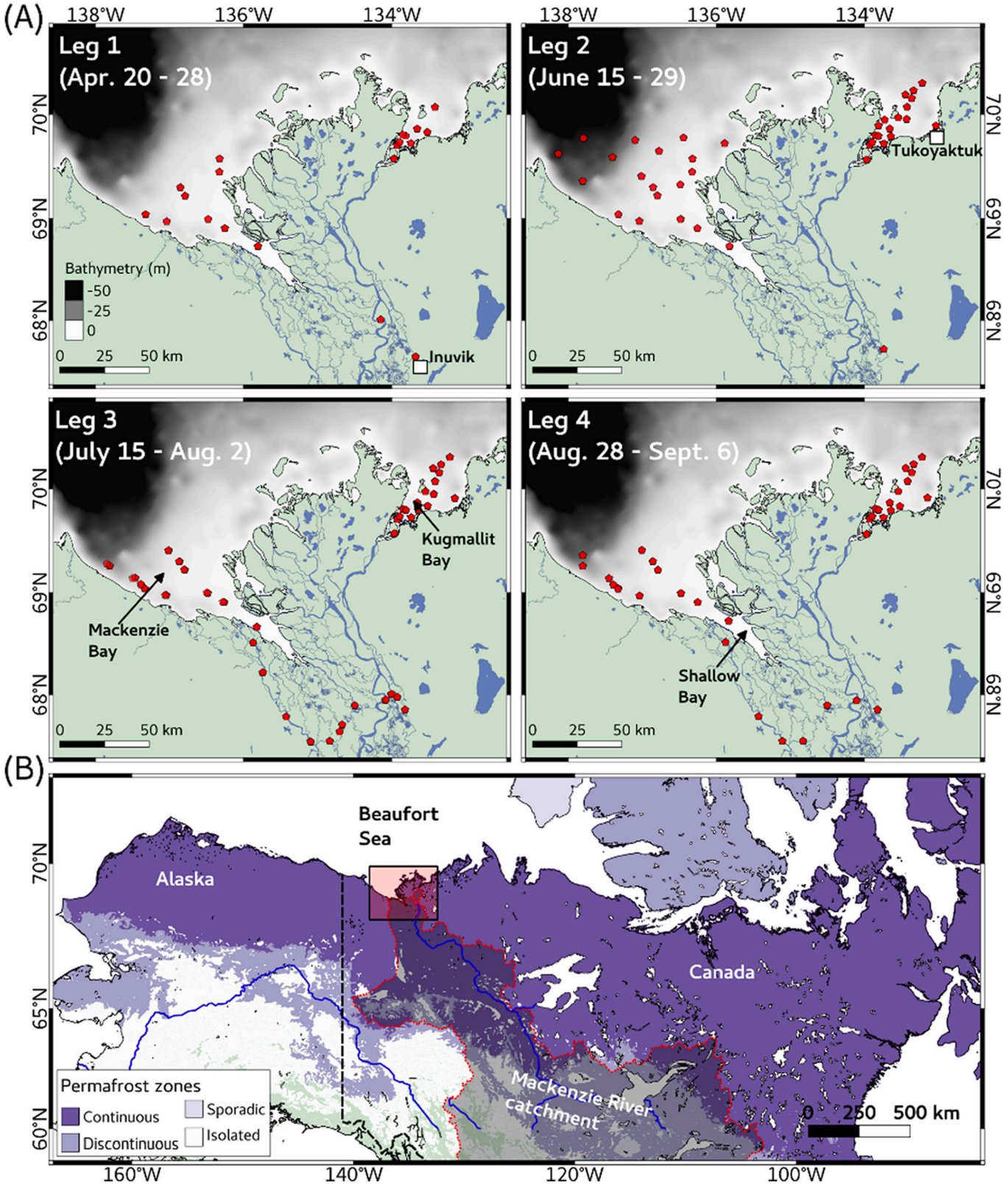

Fig. 1. (A) Sampling locations (red points) for each of the four legs. (B) Northern part of the Mackenzie River catchment and underlying permafrost zones (from Obu et al., 2019). (For interpretation of the references to color in this figure legend, the reader is referred to the web version of this article.)

scales and higher frequency. To achieve these goals, we use a unique in situ dataset that was collected during an extensive field campaign in the Mackenzie Delta region from April to September 2019.

2. Methods

2.1. Study area, sampling periods, and strategies

We carried out an extensive field campaign in the Mackenzie Delta region that consisted of four legs between April and September 2019 to capture the seasonal variability of DOM distribution and characteristics. The period covered late winter before ice break-up to late fall before ice freeze-up. The repeated sampling focused on surface waters in the two main outflow regions of the Mackenzie River: Shallow Bay and Mackenzie Bay in the west and Kugmallit Bay in the east as well as on the river channels across the delta. Many sampling locations were revisited at least once for each of the four legs (Fig. 1).

Sampling during different seasons is extremely challenging in this region due to uncertain ice cover and broken ice fields during and after ice break-up in addition to very shallow water (<5 m). To tackle these challenges, various sampling platforms were used (Fig. 2). The logistical efforts that were required for such a multi-platform operation are a part of the value and uniqueness of the dataset presented in this study.

During the first leg (April 20–28, 2019), the Mackenzie River and the coastal Beaufort Sea had a consolidated ice cover. Sampling locations were visited by a helicopter (Shallow and Mackenzie Bay) and snowmobiles (Kugmallit Bay). Water samples and CTD profiles were taken from holes drilled through the ice. During leg 2 (June 15–29, 2019), remnant ice fields were expected in Mackenzie and Shallow Bay in the early period of the open-water season, rendering the use of boats dangerous. Thus, water samples and CTD profiles were taken from a hovering helicopter, which had the advantage of allowing greater spatial coverage in a short period of time. In Kugmallit Bay, small motorboats (~6 m in length) were used and additional radiometric profile measurements, using a Compact-Optical Profiling System (C-OPS), were added. Similar boats were used during leg 3 (July 25 – August 2, 2019) and leg 4 (August 28 – September 6, 2019) for both Mackenzie and Shallow Bay. The sampling stations were located near the river mouth to capture a salinity gradient from 0 (river water) to >20 (marine-dominated water). In total, sampling was carried out at 143 stations throughout the four legs, of which 13 stations were revisited at each leg.

For a detailed overview of the complete dataset resulting from the four campaigns we refer to Lizotte et al. (2022).

2.2. In situ hydrological, biogeochemical and radiometric data

Hydrological data of the water column were acquired with a conductivity-temperature-depth probe (CTD RBR Maestro during leg 1 and a CTD RBR Concerto during legs 2 to 4). During leg 1, the CTD was manually lowered in the water through an ice hole with a velocity of <0.3 m s^{-1} and an acquisition frequency of 6 Hz, yielding a vertical resolution of a few centimetres. During legs 2 to 4, the CTD was installed on a Seabird Scientific optical package frame, which was deployed with a velocity of 0.3 m s^{-1} and an acquisition frequency of 8 Hz. Only data from downcasts were used and poor-quality profiles, that had been affected by ice-covered sensors, were removed. Atmospheric pressure observed at weather stations near the sampling locations (Aklavik, Inuvik, Shingle Point and Tuktoyaktuk) was used to tare the CTD pressure sensors. CTD profiles were smoothed and binned to a regular 0.01 m depth grid.

For DOC concentration, water samples were filtered through 0.7 µm GF/F filter, and acidified with 25 µL Suprapur HCl (10 M) on the same day of sampling. DOC samples were stored at 4 °C in the dark during transport until further analysis. Concentration of DOC was measured using high-temperature catalytic oxidation (TOC-VCPH, Shimadzu) at the Alfred-Wegener-Institute (AWI) Potsdam, Germany. Blanks (Milli-Q water) and certified reference standards (Battle-02, Mauri-09 or Super-05 from the National Laboratory for Environmental Testing, Canada) were measured for quality control.

Measurement of CDOM absorption was conducted from a water sample within 12 h of collection using an UltraPath liquid waveguide system (World Precision Instruments, Inc.) over the wavelengths ranging from 200 to 722 nm (see also Matsuoka et al. (2012) for details). Before measurement, the sample was filtered using a 0.2 µm GHP Acrodisc. To minimize temperature effects, both the sample and the reference water were kept at 4 °C for at least 30 min prior to analysis. We followed the International Ocean Colour Coordinating Group (IOCCG) Ocean Optics and Biogeochemistry CDOM protocols (Mannino et al., 2019) with a few modifications: 1) reference water with salinity ±2 relative to the sample was prepared on site a few hours before sample analysis to minimize the effect of difference in refractive index between sample and reference; 2) $a_{CDOM}(\lambda)$ was measured in flow mode, meaning that a measurement was made while water was running using a peristaltic pump (Lefering et al., 2017). While the use of a long optical cell provides a better signal, particularly within the visible spectral domain essential to SOCRS, it necessarily suffers from light saturation in the UV domain (Belz et al., 1999). To overcome this issue, an optimal cell length (i.e. 10 cm or 200 cm) was selected following an empirical relationship between optical density observed at 350 and 443 nm based on Matsuoka et al. (2012). For each sample, triplicate measurements were conducted. Each measurement was visually inspected for quality control (light saturation and microbubble effects). Suspicious spectra were discarded from our analysis. A baseline correction was applied when $a_{CDOM}(\lambda)$ averaged between 718 and 722 nm fell within the noise levels (2 times the mean of reference in the same wavelengths range). CDOM absorption measurements were fitted using the following equation:

$$a_{CDOM}(\lambda) = a_{CDOM}(\lambda_0) * e^{-S(\lambda-\lambda_0)}, \quad (1)$$

where S is the spectral slope of $a_{CDOM}(\lambda)$ between 350 and 500 nm

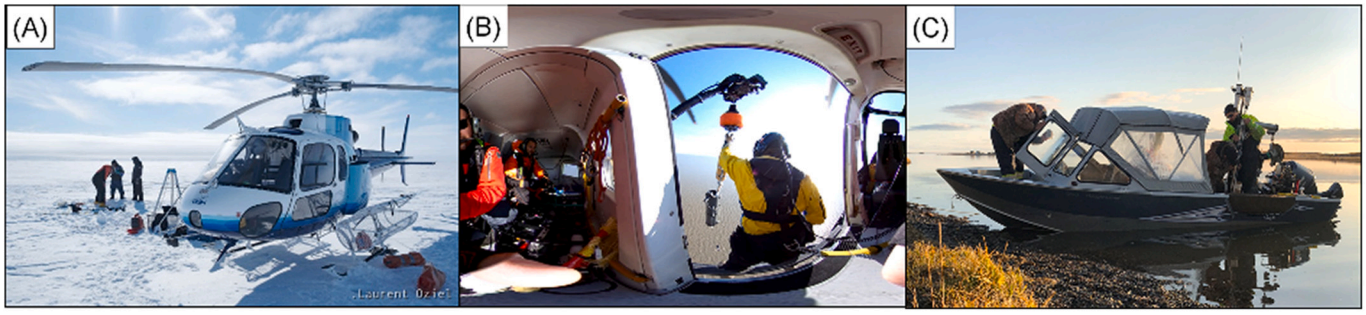

Fig. 2. Sampling platforms used during the expedition. (A) Under-ice sampling in Shallow Bay in April 2019 (credit: Laurent Oziel). (B) In-flight helicopter sampling in Shallow Bay in June 2019 (credit: Bennet Juhls). (C) Typical small boat used for sampling in Mackenzie, Shallow, and Kugmallit Bays during the open water period (credit: Martine Lizotte).

(Babin et al., 2003b; Matsuoka et al., 2012). Uncertainties for $a_{CDOM}(\lambda)$ were derived by calculating the standard deviation of the triplicates relative to the mean (of the triplicates) (Neeley et al., 2018).

2.3. Radiometric C-OPS data

Vertical profiles of downwelling irradiance ($E_d(z, \lambda)$) and upwelling radiance ($L_u(z, \lambda)$) were measured during legs 2, 3, and 4 using a C-OPS secured to an ICE-Pro frame from Biospherical Instruments, Inc. (for a detailed description see Morrow et al., 2010). During leg 2, C-OPS measurements were conducted only in Kugmallit Bay. There were no under-ice radiometric measurements using the C-OPS during leg 1. At all stations, profiling was performed until $L_u(z, \lambda)$ reached near zero and was below the detection limit of the radiometer. Moreover, at a number of locations, no C-OPS measurements were possible due to rough sea conditions. This resulted in a significantly lower number of locations with radiometric measurements compared to water samples.

In addition to profiling, above-surface downwelling incident irradiance ($E_s(0^+, \lambda)$) was measured at about two meters above sea level and was used to correct in-water $E_d(z, \lambda)$ and $L_u(z, \lambda)$ for changes in the incident light field during $L_u(z, \lambda)$ profiling (Zibordi et al., 2019). All radiometric quantities were measured at 19 wavelengths spanning from 380 to 875 nm. In-water profiles were obtained from the boat using a 3 m long pole, deployed towards the sun to avoid shading from the boat. The data that were acquired with a tilt of $>5^\circ$ were discarded (Hooker et al., 2013).

Due to the high absorption and scattering of the sampled waters and considering the relatively large dimensions of the ICE-Pro (Appendix Fig. 2), self-shading correction was required. Absorption coefficients observed in the present study were mostly outside the limits examined by Gordon and Ding (1992), suggesting that the application of the self-shading correction could be questionable. To overcome this issue, we performed Monte-Carlo simulations using the SimulO software (Leymarie et al., 2010) to determine the self-shading correction factor on $L_u(z, \lambda)$ at null depth (Gerbi et al., 2016; Leymarie et al., 2018). The exact dimensions of the ICE-Pro were simulated and virtually placed at a depth of 0.5 m. A wide range of inherent optical properties (IOPs) was considered to cover the conditions encountered in the field (Appendix Fig. 3). The simulations provide a robust relationship between the computed self-shading and the quantity $x(\lambda) = a(\lambda) + b_b(\lambda)$ for solar zenith angles $>45^\circ$ (Appendix Fig. 3), where a is the total absorption coefficient (i.e., the contributions of pure water, CDOM, algal and non-algal particles) and b_b is the total backscattering coefficient (i.e., the contributions of water molecules and particles). The shade-corrected upwelling radiance ($L_u^{corrected}(\lambda)$) can be expressed as a function of the measured radiance ($L_u^{measured}(\lambda)$) as:

$$L_u^{corrected}(\lambda) = \frac{L_u^{measured}(\lambda)}{(1 - \varepsilon(\lambda))}, \tag{2}$$

$$\varepsilon(\lambda) = 1 - e^{-0.14*(a(\lambda)+b_b(\lambda))}, \tag{3}$$

Where $a(\lambda)$ is the sum of $a_{CDOM}(\lambda)$ and $a_P(\lambda)$. $b_b(\lambda)$, which was not measured in the field, was calculated using an empirical relationship from the Malina-cruise dataset (Doxaran et al., 2012; Massicotte et al., 2020) (see Appendix). The self-shading factor is individually determined for each profile to obtain $L_u^{corrected}(\lambda)$.

Subsurface downwelling irradiance and upwelling radiance $E_d(0^-, \lambda)$ and $L_u(0^-, \lambda)$ were estimated with an iterative linear fitting of the log-transformed $E_d(z, \lambda)$ and $L_u(z, \lambda)$ vs depth z. Fitting was applied to successively greater depths until the correlation coefficient (r^2) exceeded 0.99 or until the layer thickness reached 2.5 m (Bélanger et al., 2017). Remote Sensing Reflectance ($R_{rs}(\lambda)$) was calculated following Mobley (1999) with:

$$R_{rs}(\lambda) = \frac{0.54*L_u(0^-, \lambda)}{E_s(0^+, \lambda)}, \tag{4}$$

To calculate the $R_{rs}(\lambda)$ we used the R "Cops" package (https://github.com/belasi01/Cops).

2.4. Remote sensing data

Data from the Ocean and Land Colour Instrument (OLCI) aboard the Sentinel-3A and 3B satellites were acquired at full resolution (FR) Level 1b (L1b) from https://coda.eumetsat.int (product version reference: S3IPF.PDS.004.1). We downloaded all available scenes acquired during the open water season from 1 May 2019 and 31 Oct. 2019. In this study, we tested three algorithms for atmospheric corrections: (1) The baseline atmospheric correction BAC/BIAC which is used in the Eumetsat L2 FR water product (WFR; processing baselines v.2.43 (OLCI-A) and 1.15 (OLCI-B)), based on the black pixel assumption including bright pixel correction for high-scattering waters (Moore et al., 2010), downloaded as L2 product (further referred to as WFR) from https://coda.eumetsat.int; (2) The spectral optimization algorithm Polymer v.4.13 (Steinmetz et al., 2011), which models the atmospheric contribution through a polynomial function and resolves both the atmospheric and marine signal simultaneously, processed in ython using the L1b FR (OL_1_EFR) data; and (3) the neural network approach C2RCC v.2.1, processed via GPT in SNAP v.7.0.3 using L1b FR (OL_1_EFR). System vicarious calibration (SVC) gains were applied by default for WFR and Polymer but not C2RCC. While bidirectional correction is intrinsically included in the Polymer and C2RCC atmospheric correction, this was not the case for the BAC/BIAC. Atmospherically corrected OLCI Remote Sensing Reflectance ($R_{rs}(\lambda)$) was then used as an input to two in-water retrieval algorithms. (1) The semi-analytical in-water algorithm gsmA (Matsuoka et al., 2013), which was specifically adapted from the GSM algorithm (Maritorena et al., 2002) for the retrieval of $a_{CDOM}(\lambda)$ in Arctic waters and adjusted from Moderate-resolution Imaging Spectroradiometer (MODIS) to OLCI bands for this study; and (2) the ONNS processor (Hieronymi, 2019; Hieronymi et al., 2017), which consists of several blended neural networks that are specialized for 13 different optical water classes including optically complex waters. Note that while negative reflectances were kept for gsmA they were set to 0.0001 sr^{-1} for the ONNS processor.

For match-up comparisons between in situ and satellite data, we followed the criteria proposed by Bailey and Werdell (2006), with some modifications as follows: 1) a three-by-three pixel matrix centered around each sampling location was extracted from all satellite images acquired within ± six hours of the in situ sampling time, 2) all pixels flagged for quality control by the individual atmospheric corrections were removed (see Appendix Table 1 for masks that were used) match-ups with less than five valid of a total of nine possible pixels were discarded, 4) for stations that were covered by more than one satellite acquisition within the six hours surrounding the sampling time, all available pixels were included in the analysis, relaxing the recommended criterion of ± one hour (or ideally shorter for coastal waters), 5) we calculated a median $R_{rs}(\lambda)$ of the extracted pixels for each station.

2.5. Match-up statistics

To evaluate the performance of the match-ups, we used the slope and the coefficient of determination (r^2) of the type-II linear regression between in situ and remotely-sensed $R_{rs}(\lambda)$. In addition, the MPE and the root-mean-square error (RMSE) (as in e.g. Bailey and Werdell, 2006; Matsuoka et al., 2017, 2021) were calculated as:

$$MPE\ (\%) = median\left(100*\left|\frac{X_{sat} - X_{in\ situ}}{X_{in\ situ}}\right|\right), \tag{5}$$

$$RMSE\ (sr^{-1}) = \sqrt{\frac{\sum_{n=1}^{N}[X_{sat} - X_{in\ situ}]^2}{N}}, \tag{6}$$

$$BIAS\ (\%) = \frac{1}{N} * \sum_{n=1}^{N} \frac{|X_{sat} - X_{in\ situ}|}{X_{in\ situ}} * 100, \tag{7}$$

$$Chi\ square\ mean\ (\%) = \frac{1}{N} * \sum_{n=1}^{N} \left(\sum_{j=1}^{11} \left(\frac{(K_{sat_j}(i) - K_{in\ situ_j}(i))2}{K_{in\ situ_j}(i)} \right) \right); K_j = \frac{X(\lambda_j)}{X(\lambda_{560nm})}, \tag{8}$$

where X_{sat} and $X_{in\ situ}$ are the satellite-derived and in situ measured $a_{CDOM}(443)$, respectively. i is the index of the R_{rs} wavelength (λ) and j is the index of the wavelength with the exception of the 560 band. K is the at 560 nm normalized X. For the comparison between in situ $R_{rs}(\lambda)$ and satellite $R_{rs}(\lambda)$, we used identical wavelengths, with the following two exceptions: 1) in situ 395 nm vs. satellite 400 nm and 2) in situ 765 nm vs. satellite 754 nm. Furthermore, stations that were close to the coast (e.g. river locations, Fig. 1) and might be influenced by adjacency effects were not included in the match-up comparison.

3. Results and discussion

3.1. Hydrographic seasonality of coastal waters in the Mackenzie Delta region

The Mackenzie River, like all Arctic rivers, is characterized by a nival hydrographic regime (Yang et al., 2015): low water discharge in winter is followed by a very high discharge in spring during a short freshet. In summer, the discharge is variable and mostly depends on the intensity of rain events within the catchment. The extent of river plume propagation to the Beaufort Sea strongly depends on the volume of exported water, but also on other factors including wind and ocean currents (Ehn et al., 2019; Macdonald et al., 1995; Mulligan and Perrie, 2019).

During the four legs, we collected hydrographic data for the complete water column. Fig. 3 shows the in situ surface salinity distribution in the coastal Mackenzie Delta region during the four expedition legs in 2019. The variability in stratification of the coastal waters is shown in Fig. 4. In April (leg 1), when the coastal waters of the Beaufort Sea were still ice-covered, solely fresh river water was found below the ice, with low salinity ranging between 0.11 and 0.17. Even at the distant offshore stations (>50 km from the river mouth), no elevated salinity from marine waters was observed (Fig. 3A). No significant vertical stratification was observed within the fresh waters (Figs. 4A & 4E).

In June (leg 2), the fresh river water plume displayed the greatest extent of the three legs during the open water period (Fig. 3B). Whereas in the western bay (Mackenzie and Shallow Bays), the river plume propagated over large areas with low salinities (<5) observed >100 km away from the river mouth, the plume extent in the eastern bay (Kugmallit Bay) was limited to only a few tens of kilometres from the river mouth. The larger plume in the Mackenzie Bay (west) compared to the Kugmallit Bay (east) is likely a direct result of a larger freshwater reception in the Mackenzie Bay.

In late July/early August (leg 3), the river plume extent was substantially smaller compared to that of leg 2. Higher salinity waters (>20) were found in the eastern sector of Mackenzie Bay and in the northern sector of Kugmallit Bay. At the end of August/ beginning of September (leg 4), the plume extent with low salinity water once again increased and high salinity waters were found only in the most offshore stations.

3.2. Seasonal variability of dissolved organic matter

The carbon content of the dissolved organic matter was measured as DOC. The colored fraction of organic matter was measured as the light

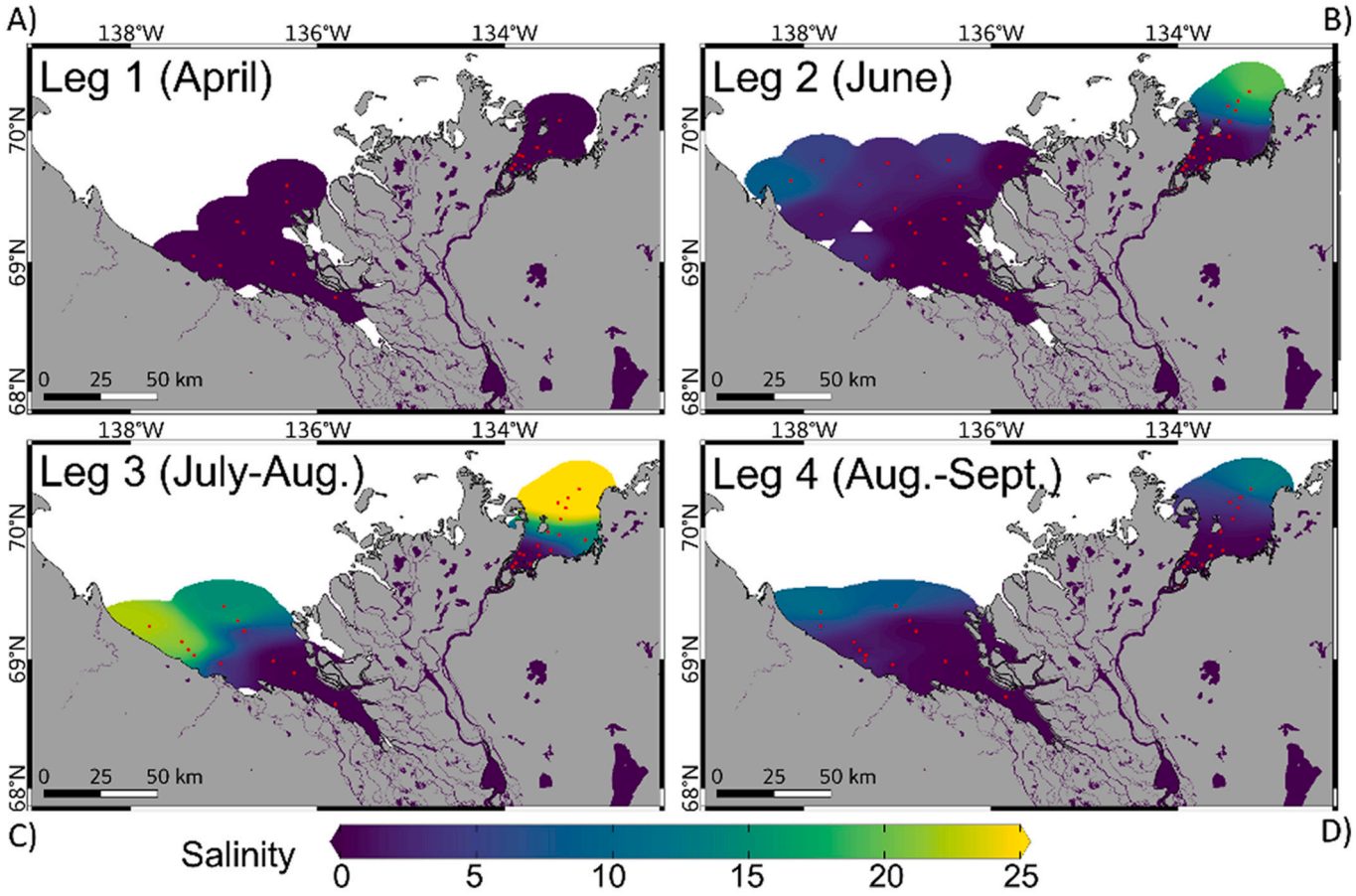

Fig. 3. Spatial distribution of the in situ surface salinity in the coastal waters for leg 1 (A), leg 2 (B), leg 3 (C) and leg 4 (D).

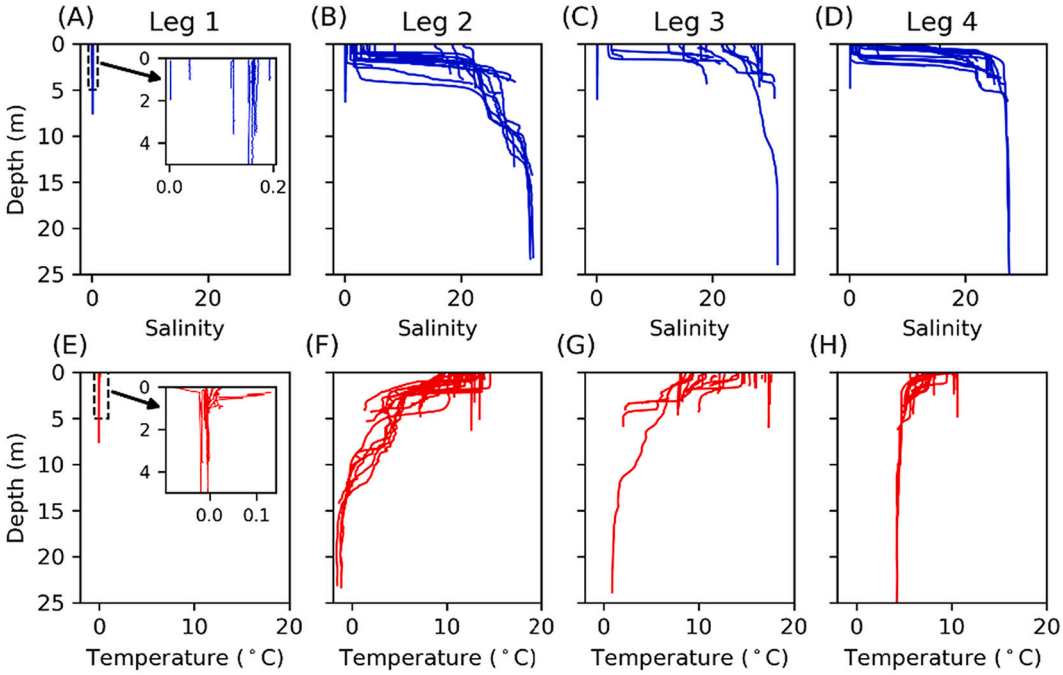

Fig. 4. Depth profiles of salinity (A-D) and temperature (*E*-H) for the four expedition legs. For leg 1 (A & E) the inset figures show lower value ranges.

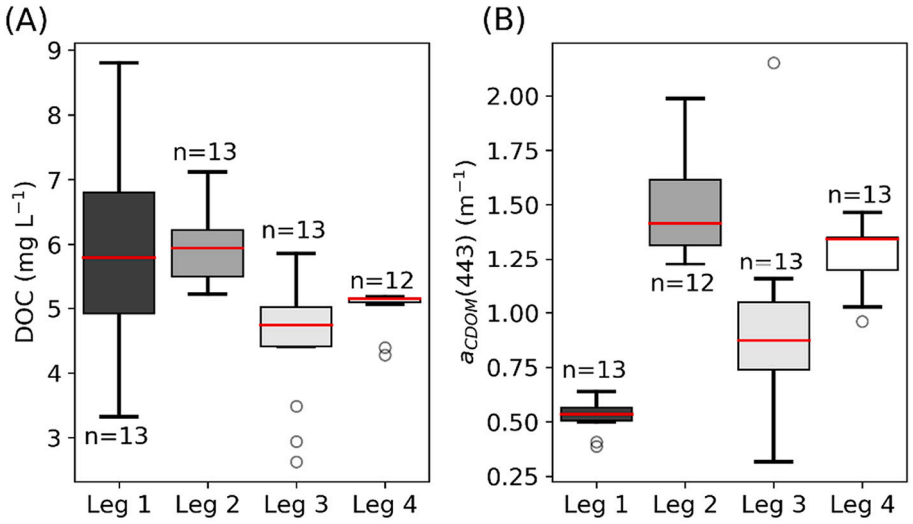

Fig. 5. Main statistics for surface DOC concentration (A), and surface CDOM absorption at 443 nm (B) associated with the stations that were revisited during all four expedition legs (n = 13).

absorption by CDOM ($a_{CDOM}(\lambda)$). Fig. 5 shows the observed ranges of CDOM and DOC for stations that were revisited during all four expedition legs ($n = 13$). Concentrations of DOC during leg 1 (under ice samples) showed the highest range from 3.3 to 8.8 mg L^{-1} with a mean value of 5.7 mg L^{-1}. The mean DOC concentration for leg 2 (5.8 mg L^{-1}) was the highest among all legs, while the mean DOC concentration for leg 3 was the lowest (4.1 mg L^{-1}). During leg 1, $a_{CDOM}(443)$ was lowest compared to all other legs and, unlike DOC concentrations, showed a very narrow range (from 0.39 to 0.73 m^{-1}). Seasonal patterns of DOC and $a_{CDOM}(443)$ were, however, similar with lowest $a_{CDOM}(443)$ during leg 1 (mean of 0.55 m^{-1}) and the highest during leg 2 (mean of 1.41 m^{-1}). DOC and $a_{CDOM}(443)$ in the study area are mostly dependent on the discharge and resulting input of organic matter by the Mackenzie River. The lower discharge during leg 3 compared to leg 4 (Fig. 13) explains the lower DOC and $a_{CDOM}(443)$ during leg 3 compared to leg 4.

Observed DOC concentrations and $a_{CDOM}(443)$ showed a strong relationship with salinity for all expedition legs during the open water period (Fig. 6) when excluding stations with salinity <0.5. The mixing line for both DOC and $a_{CDOM}(443)$, varied slightly between the expedition legs in slope and intercepts (represented by grey areas in Fig. 6). Zero salinity (fresh water) intercept of the mixing lines (red symbols in Fig. 6), including the variability between the legs, are within or close to the observed river concentrations. The highest DOC and $a_{CDOM}(443)$ along the salinity gradient were observed during leg 2, whereas the lowest DOC were observed during leg 3 and lowest $a_{CDOM}(443)$ during leg 4.

The strong relationship of DOC and $a_{CDOM}(443)$ to salinity is consistent with earlier studies that reported conservative mixing behaviour of DOM in river-influenced coastal Beaufort Sea (Emmerton et al., 2008; Matsuoka et al., 2012; Osburn et al., 2009) and clearly

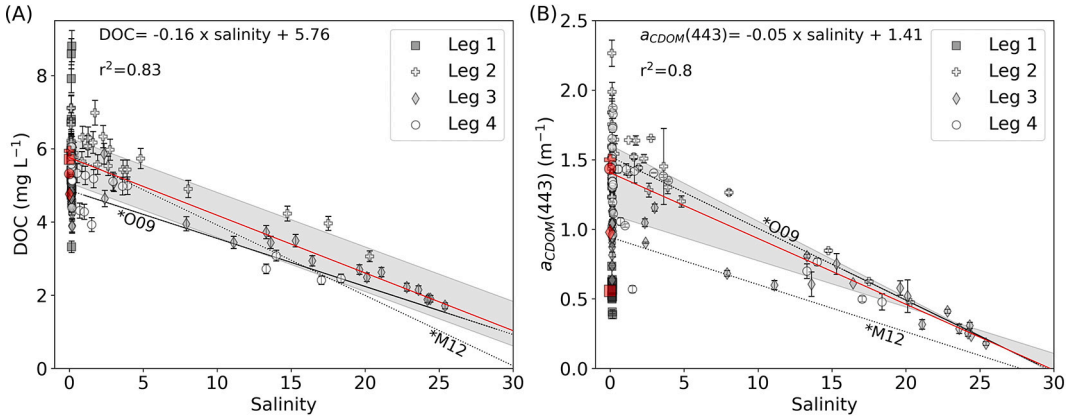

Fig. 6. Relationships between DOC and salinity (A) and $a_{CDOM}(443)$ and salinity (B) for all samples from four expedition legs. The red lines show the regressions for the samples from legs 2, 3, and 4 (samples with salinity <0.5 were excluded). Red symbols show the mean DOC (A) and mean $a_{CDOM}(443)$ from each leg (B) for samples with salinities <0.5 (river water). The grey filled areas show the range of relationships, when calculated separately for each leg. Reported regression lines from Osburn et al. (2009) for the coastal Beaufort Sea (*O09) and from Matsuoka et al. (2012) for the offshore Beaufort Sea (*M12) are given for comparison. Note that for leg 1 no salinities >0.5 were observed and thus no regression line between salinity and DOC or $a_{CDOM}(443)$ was considered. (For interpretation of the references to color in this figure legend, the reader is referred to the web version of this article.)

identifies terrigenous material as the dominant source of DOM. Larger amounts of autochthonously produced DOM from primary production or additional release of DOC by coastal erosion could explain positive deviations from the hypothetical mixing line (regression line in Fig. 6). In contrast, degradation and flocculation processes could explain deviations below the hypothetical mixing line. The main driver for the seasonal variability of the mixing line slope is likely the seasonal variation of DOC and $a_{CDOM}(443)$ in the Mackenzie River, which defines the initial concentration at zero salinity which then propagates to the coastal waters and the Beaufort Sea shelf. Thus, the seasonal variation of the river water DOC and $a_{CDOM}(443)$ can also be a reason for strong deviations from the mixing line along the salinity gradient when water sampled is influenced by different initial concentrations. This likely also causes the generally weak relationship of DOC and $a_{CDOM}(443)$ to salinity in the salinity range between 0 and 5.

Only for leg 4 is the mixing line lower compared to leg 3 (not shown), despite river DOC and $a_{CDOM}(443)$ being higher during leg 4. The found relationship between DOC and salinity (combined legs 2 to 4, red line in Fig. 6A) agrees well with the relationships reported in Osburn et al. (2009) and Matsuoka et al. (2012). The relationship between $a_{CDOM}(443)$ and salinity (combined legs 2 to 4, red line in Fig. 6B) agrees well with Osburn et al. (2009) whereas the relationship reported by Matsuoka et al. (2012) is substantially different.

3.3. DOC-CDOM relationship

Concentrations of DOC in river-influenced water can be estimated from $a_{CDOM}(\lambda)$ as supported by multiple studies reporting a strong relationship between DOC and CDOM on Arctic shelf seas (Gonçalves-Araujo et al., 2015; Juhls et al., 2019; Matsuoka et al., 2012, 2017; Pugach et al., 2018). For an accurate quantification of DOC from CDOM in the fluvial-marine transition zone, a robust relationship must be developed that addresses the knowledge gap associated with nearshore waters and changing seasons. Variations of the DOC-CDOM relationship can result from geographical and seasonal differences in sampling, as well as the range of concentration of DOM and CDOM used to infer the relationships. The identification and characterization of this variability is a prerequisite to define the limits of validity of these relationships. In order to evaluate limitations of this relationship, we compared the relationship of this study to previously reported DOC-CDOM relationships from other Arctic shelves.

Fig. 7 shows the relationship between DOC and $a_{CDOM}(443)$ for all the samples from this study. We found a strong non-linear relationship

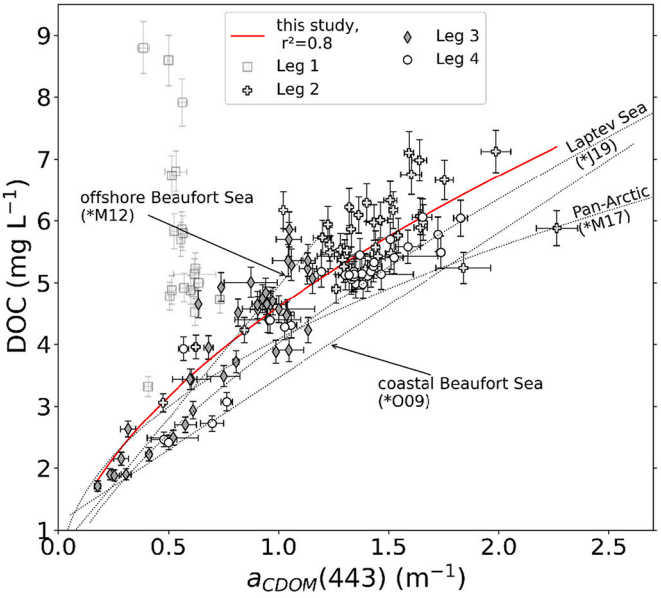

Fig. 7. Relationships between DOC and $a_{CDOM}(443)$ with their measurement uncertainties. The red solid line shows the regression for samples from this study (only legs 2, 3 and 4) ($DOC = 4.61 \times a_{CDOM}(443)^{0.546}$). The dashed black lines shows the relationships reported by Osburn et al. (2009) for the coastal Beaufort Sea (*O09), Matsuoka et al. (2012) for the offshore Beaufort Sea (*M12), Matsuoka et al. (2017) for the pan-Arctic (*M17), and Juhls et al. (2019) for the Laptev Sea (*J19). (For interpretation of the references to color in this figure legend, the reader is referred to the web version of this article.)

($r^2 = 0.8$) considering only legs 2 to 4 during the ice-free period. The relationship of samples from leg 1 differed substantially. Leg 1 showed high variability in DOC but a low variability in $a_{CDOM}(443)$ (light grey squares in Fig. 7). This result indicates that the relationship, which was developed from samples during the open water period, cannot be used to estimate DOC from CDOM during the ice-covered period and also may not be representative of the shoulder seasons in spring and fall. The seasonal differences of the relationship can be caused by changes in source, composition and degradational state of the DOM (e.g. Juhls et al., 2020).

Generally, the DOC-CDOM relationship for the open water period (combined legs 2–4) is similar to previously reported relationships for

the Lena River – Laptev Sea transitional zone (Juhls et al., 2019), offshore Beaufort Sea (Matsuoka et al., 2012), and pan-Arctic (Matsuoka et al., 2017). The relationships from Matsuoka et al. (2012, 2017) differ substantially from the relationship of the combined legs 2, 3 and 4 of this study in high concentration DOC ranges (>5 mg L^{-1}), which is likely caused by a lack of samples from the river mouth waters with high DOC concentration that were used by Matsuoka et al. (2012). This is confirmed by a close resemblance between the DOC–CDOM relationship from this study and the DOC–CDOM relationship from Juhls et al. (2019), which was developed using a large number of samples from river, coastal, and offshore waters in the Laptev Sea region. The resemblance between relationships from the Beaufort Sea region and those from the Laptev Sea region may reflects a regional similarity of the DOM lability and susceptibility to microbial and photochemical reactions and flocculation. The comparison of reported relationships with the cross-domain coverage of the relationship from this study endorsed the use of non-linear models for an optimal fit. Seasonal differences in DOM characteristics that result in changing relationships between DOC and CDOM further complicate the development of a robust model. Nevertheless, the non-linear model established in this study captures most of the DOC-CDOM relationship across ice-free seasons.

3.4. Evaluation of Satellite Ocean Colour Remote Sensing data

To evaluate the performance of SOCRS in the coastal waters of the Mackenzie Delta – Beaufort Sea region, we first tested three available atmospheric corrections (WFR, C2RCC v.2.1, and Polymer 4.13) by comparing in situ $R_{rs}(\lambda)$ versus satellite $R_{rs}(\lambda)$. We also tested two CDOM retrieval algorithms (ONNS and gsmA) using the $R_{rs}(\lambda)$ retrieved from each of the three tested AC's. Given that the surface of the water was covered by ice during leg 1, this analysis was only considered for legs 2, 3 and 4.

3.4.1. Atmospheric correction

Fig. 8 shows the match-up comparisons between in situ $R_{rs}(\lambda)$ and the satellite-derived $R_{rs}(\lambda)$. While all three AC's show only moderate performances regarding slope and coefficient of determination (r^2), overall, the Polymer algorithm provided the best performance with a mean bias of 9.25% (mean of all bands with exception of the 709 nm), a root mean square error (RMSE) of 0.003 sr^{-1} (mean of all bands with exception of the 709 nm, and the lowest Chi squared mean of 4.5% (mean of all bands with exception of 709 nm) compared to the other two AC's (Fig. 8, Table 1). The low slopes (mean of 0.468) indicate that Polymer does not capture the dynamic range of the in situ $R_{rs}(\lambda)$, leading to an overestimation at low values and underestimation at high values, especially at shorter wavelengths (Appendix Table 2).

We excluded the 709 nm band from the reported mean statistics since it showed exceptionally worse performance compared to all other bands, which might result of poor representativeness of internal model or training dataset to the waters of this study or of the poor water vapor correction at this band. It is noted that the Polymer algorithm retrieved $R_{rs}(\lambda)$ at more stations ($n = 60$) than the other AC's (WFR $n = 46$, C2RCC $n = 58$). The lower number of retrieved $R_{rs}(\lambda)$ for WFR and C2RCC was caused by flagging values that were outside of validity bounds for these AC algorithms. However, it is noted that the use of flags is subjective, might be related to algorithm maturity and raised flags do not necessarily mean that the retrieved information is out of scope for an successive algorithm application. Red bands, which have the highest $R_{rs}(\lambda)$ range, showed the best performance for all tested AC's.

Table 1
Performance of different AC's as a mean of all wavelengths: match-ups between in situ and satellite $R_{rs}(\lambda)$. Best performing AC for each statistical parameter are highlighted in grey.

AC	N	Slope	r^2	MPE (%)	RMSE (sr^{-1})	Bias (%)	Chi squared mean (%)
WFR	45.6	1.325	0.231	45.123	0.005	49.018	12.923
C2RCC	57.1	1.202	0.281	32.87	0.005	49.682	12.127
Polymer	59.5	0.468	0.26	40.842	0.003	9.248	4.473

Overall, the match-up comparison indicated rather poor performances of all three AC's in the near-shore waters of the Mackenzie Delta - Beaufort Sea region. Additionally, they showed significantly different $R_{rs}(\lambda)$ retrieval results on same pixels, which cannot be solely explained by varying implementation of the bidirectional correction. However, the shape of the $R_{rs}(\lambda)$ spectra were relatively well retrieved throughout all AC algorithms and similar to the $R_{rs}(\lambda)$ spectra from in situ measurements (Fig. 9). Note, that this evaluation is based on the measurements during the ice-free period.

The evaluation of AC's in extremely optically complex waters as in this study is difficult due to at least two factors. First, an evaluation requires a high accuracy of in situ measured $R_{rs}(\lambda)$ (Bélanger et al., 2017), which is challenging to achieve in hydrographically and optically complex waters. This is because subsurface radiometric measurements for the retrieval of $R_{rs}(\lambda)$ require extrapolation of $L_u(z, \lambda)$ to just below the sea surface ($z = 0^-$). The quality of the $R_{rs}(\lambda)$ estimates at the 0^- m depth strongly depends on whether the layer that was used for the extrapolation is representative of the layer from which water-leaving radiance is sensed by a satellite ocean colour sensor. If multiple water layers with different optical properties are present, it is necessary to restrict the extrapolation to the uppermost water layer. At some locations, only a very thin layer (<50 cm) of turbid river waters overlaid transparent saline waters (Fig. 4) with distinctly different optical properties. This also reduced the total thickness of the layer that can be used

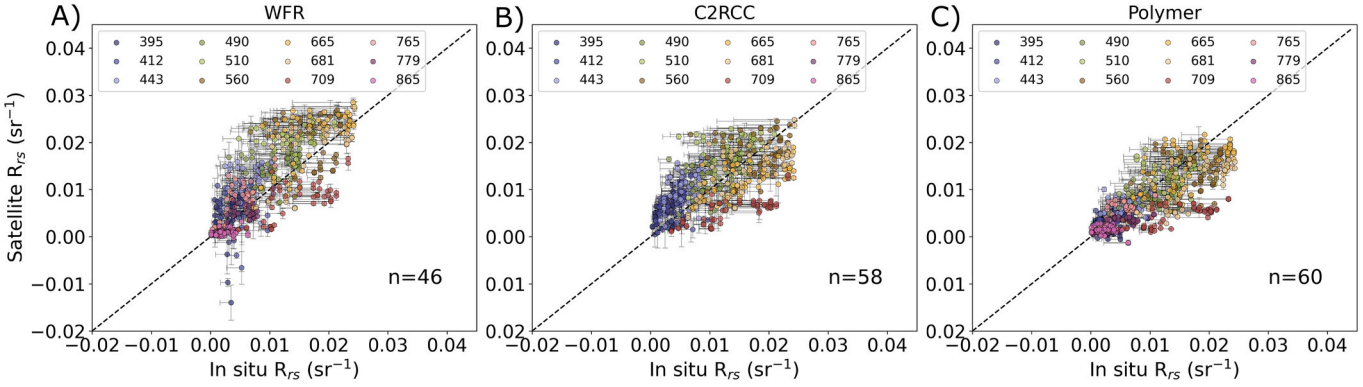

Fig. 8. Match-up of in situ and satellite $R_{rs}(\lambda)$ after using the AC's WFR (A), C2RCC (B) and Polymer (C). Only the stations where in situ measurements could be paired with satellite acquisitions (± 6 h of sampling period) were used. The error bars along the y axis show the standard variation within pixels used for the match-up. The error bar along the x axis shows the range of $R_{rs}(\lambda)$ for uncorrected and our applied shadow correction.

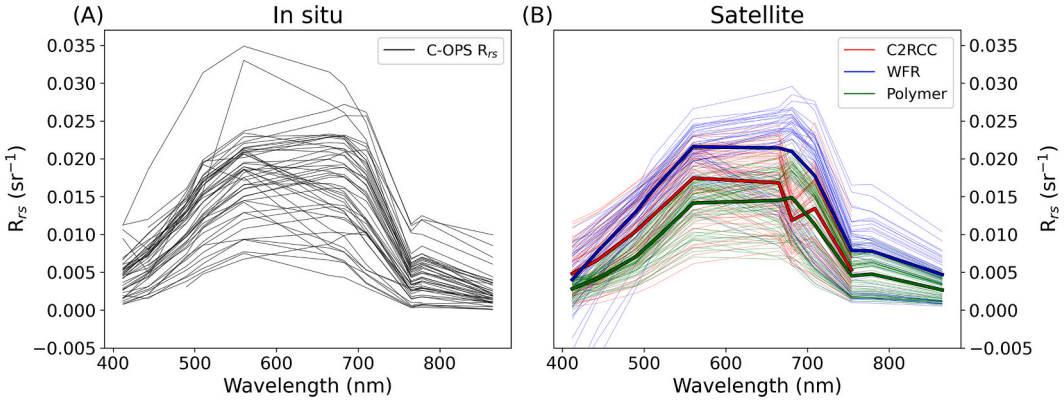

Fig. 9. $R_{rs}(\lambda)$ spectra derived from in situ measurements (A) and from satellite using three different AC algorithms (B), where the thick colored line shows the mean of each AC algorithm.

for $L_u(z)$ extrapolation, which complicates the accuracy of extrapolation, especially for blue and NIR bands where the signal is smallest. Using small vessels, measurements often took place at high tilt angles, reducing the number of data points that were used and resulting in a weaker regression for the extrapolation of $L_u(z)$ to the water surface. The minimum at 443 nm for some $R_{rs}(\lambda)$ spectra (Fig. 9a) is a distinct example for in situ $R_{rs}(\lambda)$ uncertainties. Additionally, the inherent optical properties found in this study (extreme scattering, strong absorption) are mostly outside the limits of traditional self-shading corrections (e.g. Gordon and Ding, 1992). The self-shading correction has a significant impact on the $R_{rs}(\lambda)$ (x-axis error bars in Fig. 8) and thus may also introduce higher uncertainties. Second, waters within the fluvial-marine transition zone can be highly turbulent and a time difference of even just a few minutes can be sufficient to explain the observed deviation between satellite and in situ $R_{rs}(\lambda)$. For the match-up analysis, we considered all pixels from satellite images that were acquired within ±6 h of the sampling timing for in situ measurements. Although no distinct patterns of a time dependency of the match-up performance were observed, the influence of rapidly changing water masses cannot be entirely excluded.

However, there are a number of additional challenges for AC algorithms in high latitudes and turbid waters, particularly related to CDOM retrievals. These challenges include large sun zenith angles, a relatively high air mass, adjacency effects from snow and ice, very low marine reflectance, sensitivity to subvisible clouds and dust, and the relative importance of blue bands, where most AC algorithms exhibit larger biases (IOCCG, 2010; Tilstone et al., 2021).

Our AC performance test agrees with other reported OLCI AC comparisons for coastal waters (Gossn et al., 2019; Mograne et al., 2019; Renosh et al., 2020). Mograne et al. (2019) evaluated five different OLCI AC's (WFR, C2RCC v.2.1 and Polymer v. 4.10, among others) for turbid coastal waters. They concluded that C2RCC and Polymer performed best. The weaker performance of the match-up results in our study compared to Mograne et al. (2019) could be explained by a higher optical complexity of the waters in our study which potentially increases the uncertainty of the in situ $R_{rs}(\lambda)$. Nonetheless, to our knowledge, the present study shows the first extensive in situ radiometric data that provide insights into the performance of recent atmospheric correction

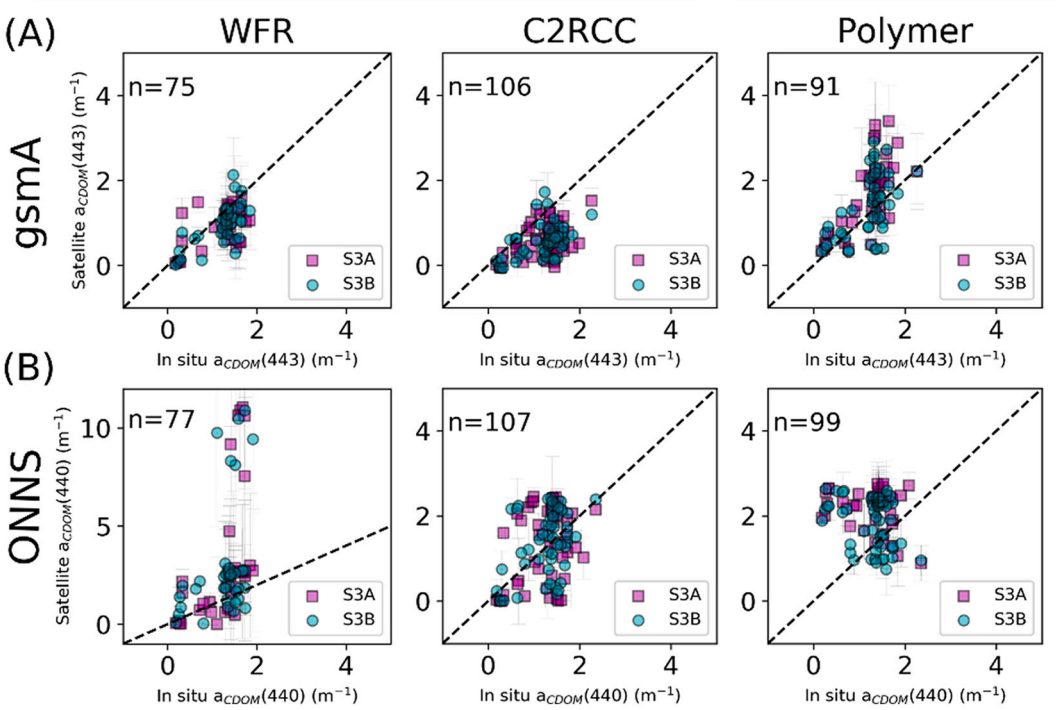

Fig. 10. Match-up comparison between in situ CDOM and satellite-derived CDOM for the three tested AC's and two CDOM retrieval algorithms: (A) gsmA, (B) ONNS.

algorithms in optically-complex Arctic waters near a large river mouth.

3.4.2. CDOM retrieval performance

In this study, we tested two in-water CDOM retrieval algorithms (gsmA and ONNS) applied to $R_{rs}(\lambda)$ data retrieved using the three different AC algorithms (Fig. 10). The two algorithms apply fundamentally different approaches for the retrieval of CDOM. gsmA is based on a mathematical iteration method to minimize differences between observed (satellite) $R_{rs}(\lambda)$ and modeled $R_{rs}(\lambda)$ using varying absorption and backscattering coefficients (Maritorena et al., 2002). In contrast, ONNS employs blended various neural network algorithms each of which was trained with an optimized scope of relations between the optical properties of water constituents and $R_{rs}(\lambda)$ (Hieronymi et al., 2017). The results of match-up comparisons with in situ CDOM measurements showed that the gsmA algorithm's performance was more stable across the three AC's (Table 2). The use of the gsmA in combination with the Polymer AC resulted in the best match-up performance (slope = 1.08, r^2 = 0.4, MPE = 35.72%, RMSE = 0.71 m^{-1}). The CDOM retrieval using the gsmA in combination with WFR AC and ONNS in combination with C2RCC showed the next highest performance statistics. The combination of ONNS with WFR resulted in a poor performance (slope = 2.82, r^2 = 0.19, MPE = 49.1%, RMSE = 3.39 m^{-1}) with large deviations from the 1 to 1 line. This may be related to excessive provision of negative reflectances (Fig. 9b), which results in out of scope values within the optical water type (OWT) classification of the ONNS algorithm. Consequently, and with respect to ONNS, the spectral shape is most important and partly explains poor OWT classifiability and CDOM retrieval capacity. The use of fewer bands for gsmA compared to ONNS (that uses all bands between 400 and 865 nm) could explain the differences in performances. For none of the AC and CDOM retrieval combinations were significant differences between Sentinel-3 A (S3A) and Sentinel-3 B (S3B) observed.

Results from in this study indicate higher errors (~35% MPE if using Polymer AC) compared to Matsuoka et al. (2013) reporting a ~ 20% MPE for coastal waters of the Beaufort Sea and Matsuoka et al. (2017) reporting a ~ 10% MPE for pan-arctic offshore waters using the gsmA CDOM retrieval using MODIS satellite data. It should be noted however that the ranges of $a_{CDOM}(443)$ observed in this study were substantially higher compared to other reported match up exercises. Most stations that were sampled in this study were near the Mackenzie River mouth, resulting in higher CDOM and sediment load and overall higher optical complexity compared to previous studies. Lower retrieval performances for the near-shore waters are thus expected.

3.4.3. Retrieving DOC concentrations from CDOM

DOC concentrations can be estimated using ocean colour data when retrieved CDOM absorption is accurately retrieved and applied to a robust empirical relationship between DOC concentration and CDOM. We merged the available in situ data including those obtained for the Mackenzie Delta - Beaufort Sea region from Osburn et al. (2009) and Matsuoka et al. (2012) and this study and established a new DOC-CDOM relationship:

$$DOC = 4.4907 * a_{CDOM}(443)^{0.578} \quad (9)$$

Table 2
Performance statistics of CDOM retrieval using the three tested AC algorithms and two CDOM retrieval algorithms.

AC	Algorithm	Slope	r^2	MPE (%)	RMSE (m^{-1})
WFR	gsmA	0.6	0.2	38.2	0.49
	ONNS	2.82	0.19	49.1	3.39
C2RCC	gsmA	0.4	0.22	123.54	0.76
	ONNS	0.64	0.14	37.89	0.78
Polymer	gsmA	1.08	0.4	35.72	0.71
	ONNS	−0.29	0.06	40.52	1.11

This relationship includes data obtained from river, coastal and offshore waters and thus enables the retrieval of DOC concentration across the fluvial-marine transition zone within its validity of 0.0197 $m^{-1} < a_{CDOM}(443) < 2.612\ m^{-1}$, and 0.593 mg L^{-1} < DOC <7.12 mg L^{-1}. However, the relationship is limited to salinities <25, where river water is the dominant source of DOC. Fig. 11 shows the match-up result between in situ and the satellite-derived DOC concentrations using the best performing AC and CDOM retrieval (i.e., Polymer-retrieved $R_{rs}(\lambda)$ applied to gsmA) through the new DOC-CDOM relationship. The satellite-derived DOC concentrations lay within a 20.5% error (1.45 mg L^{-1}) of the in situ data as a whole. The use of our merged DOC-CDOM relationship substantially improved the retrieval of DOC concentrations for near-shore waters of the Mackenzie Delta - Beaufort Sea region compared to relationships that were developed for a specific area and sampling period.

3.5. Synoptic satellite maps of DOC concentrations

The high temporal resolution of polar orbiting satellites (such as OLCI) provides a powerful tool for synoptic monitoring of surface water DOC distribution and river plume propagation for the entire sea-ice free season. Fig. 12 shows satellite maps of the surface water DOC concentrations for the wider Mackenzie Delta – Beaufort Sea region between May and mid October 2019 using Polymer, gsmA and our merged DOC-CDOM relationship (Eq. 9) with an estimated uncertainty of 20.5% (Fig. 11).

The maps in Fig. 12 show strong variability in the extent of the Mackenzie River plume with higher DOC concentrations throughout the open water season. In the first half of May, sea ice still covered the water surface in the near-shore areas and most of the Beaufort Sea Shelf. Nevertheless, in the open water area between landfast and pack ice, the onset of the river plume propagation initiated by the river ice breakup was visible. The spatial distribution of the DOC-rich river plume further expanded and was highest during the first half of June. Besides the farthest northward propagation, waters with high DOC concentrations (>1.5 mg L^{-1}) were transported to the northwest and the northeast. The extent of the plume rapidly decreased in the second half of June. This is likely associated with the termination of the spring freshet coupled with dilution by low-DOC oceanic water. The decrease in DOC concentrations could be partly due to the higher biological and photochemical lability of DOM particularly during the spring freshet (Amon et al., 2012; Mann et al., 2012; Osburn et al., 2009). Later in the year, the extent of the plume was significantly smaller and varied only slightly. High concentrations (>4 mg L^{-1}) were restricted to a relatively narrow band around the Mackenzie Delta (<5 km).

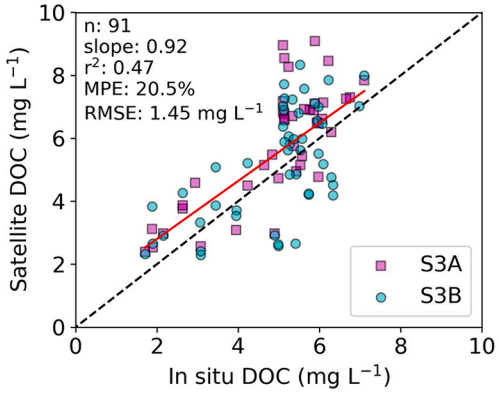

Fig. 11. Performance of DOC retrieval using Polymer AC in combination with the gsmA CDOM retrieval and the merged DOC-CDOM relationship for the Beaufort Sea (Eq. 9). The red line shows the linear regression. (For interpretation of the references to color in this figure legend, the reader is referred to the web version of this article.)

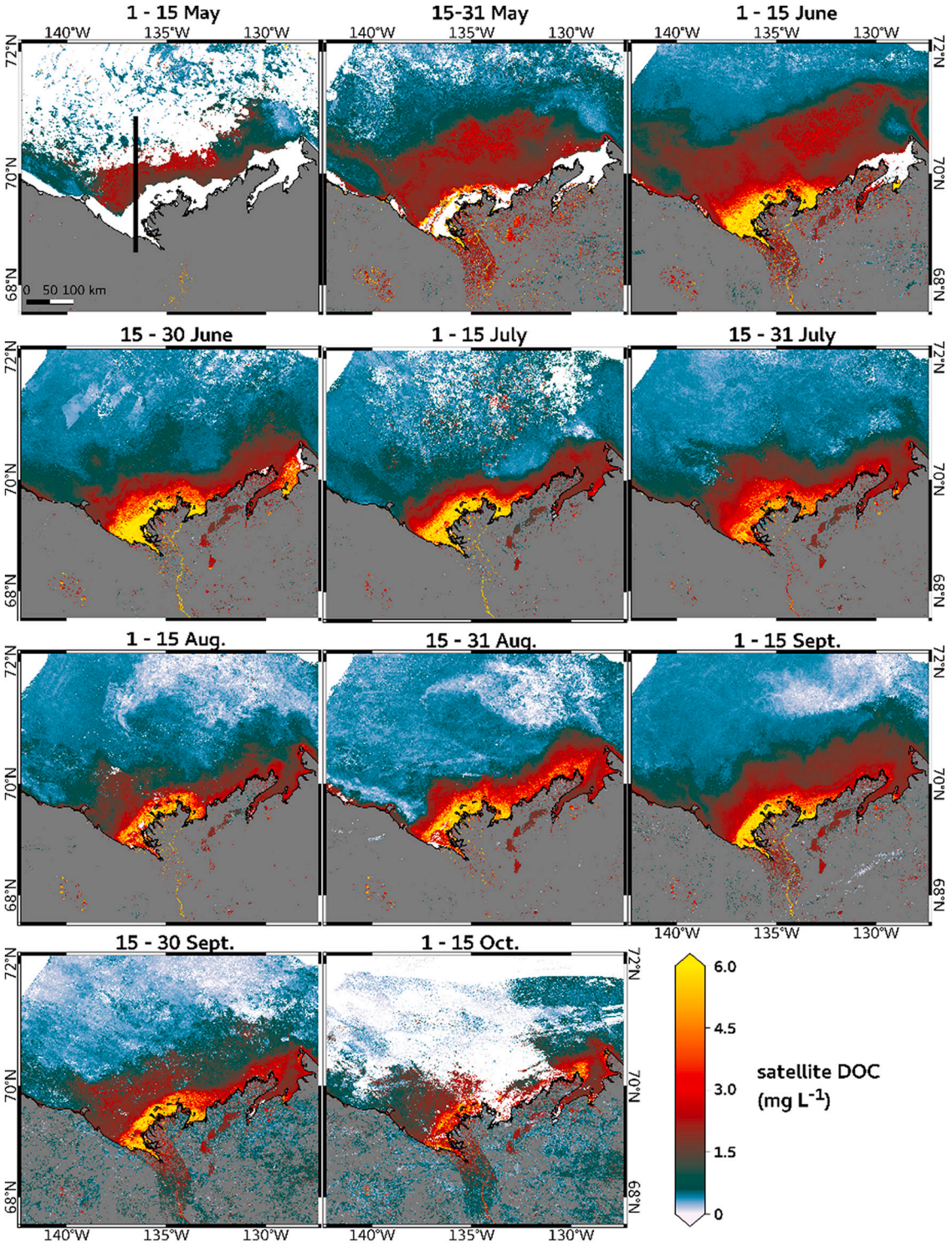

Fig. 12. Half-month mean surface water DOC concentration of the Mackenzie Delta – Beaufort Sea region. The Polymer AC, in combination with the gsmA CDOM retrieval, was applied to all available S3 OLCI data. DOC concentration was calculated using Eq. 9. The black line in the upper left map shows the position of the transect described in Fig. 13. White areas correspond to sea-ice or cloud cover.

Fig. 13A illustrates the DOC concentrations along the 136.4°W meridian (from 69°N to 71°N, black line in Fig. 12) during the open water season from May 1 to October 1, 2019. Variations in DOC along the south-north transect over time demonstrate the impact of Mackenzie runoff (Fig. 13B) on the northward river plume propagation over the Beaufort Sea Shelf. The highest concentrations, as well as the farthest northward propagation of DOC-rich waters, correspond to the peak of the Mackenzie River water level (as a proxy for discharge). The satellite-derived DOC concentrations of the southernmost part of the transect corroborate the observed in situ seasonal variation with the highest DOC during leg 2, low concentrations during leg 3, and moderate concentrations during leg 4. At the beginning of the open water period, the concentration and propagation of DOC appear to be dependent entirely on the Mackenzie River runoff due to the large volume of water that

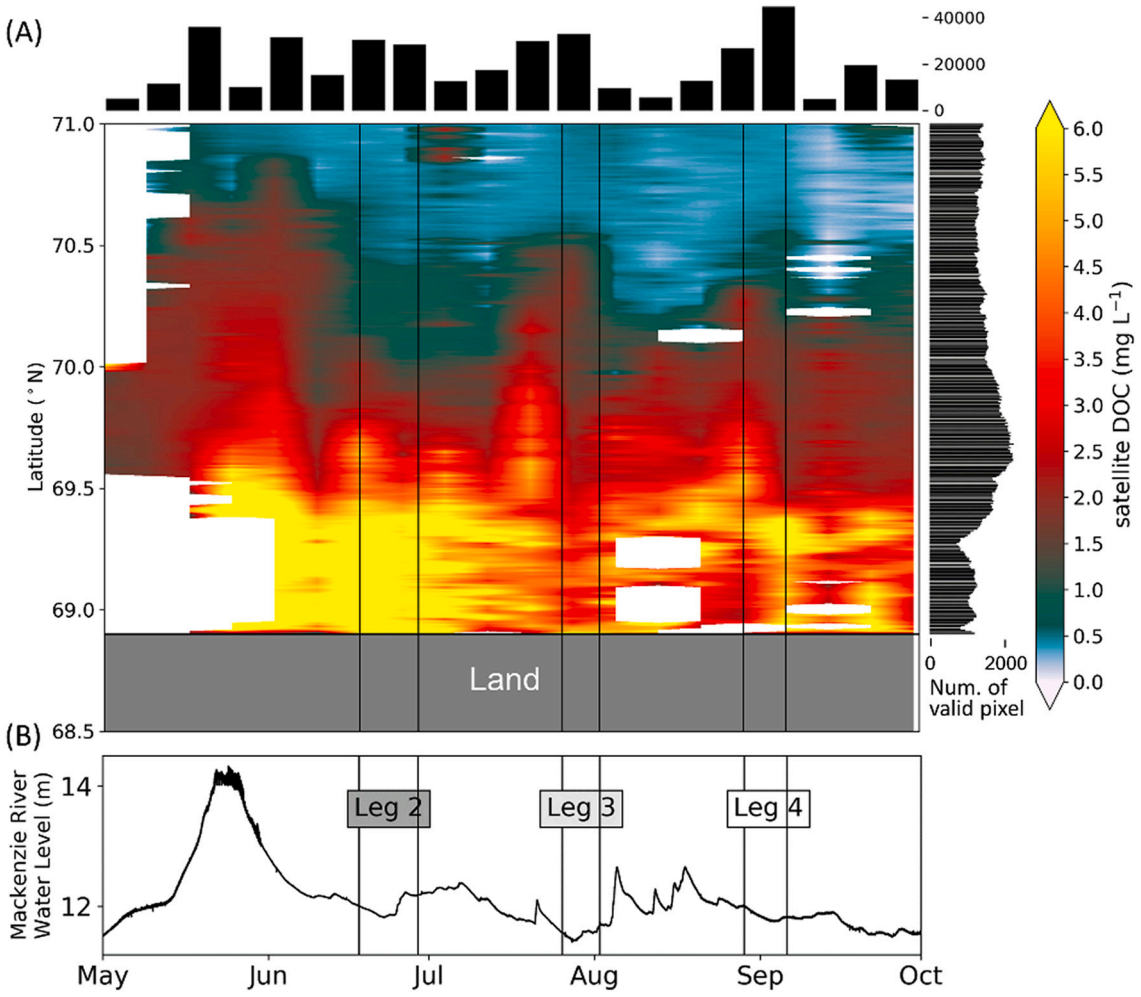

Fig. 13. (A) DOC concentrations along the 136.4°W meridian (see Fig. 12, consisting of 313 × 9 pixels) from 68.5 to 71°N from May to October 2019. All available OLCI acquisitions were processed with the Polymer AC. $a_{CDOM}(443)$ was retrieved using the gsmA algorithm. The DOC concentrations were estimated using the merged DOC-CDOM relationship (Eq. 9). To account for masked satellite data due to cloud and ice cover, transect medians of eight days were used. The number of valid pixels for each eight-day median is displayed in the upper histogram and the number of valid pixels along a latitudinal grid is shown in the histogram on the right. Appendix Fig. 1 shows the number of observations that were used for each grid point of this fig. (B) shows the provisional water level of the Mackenzie River (East Channel) at Inuvik (Station 10LC002) for May to October 2019 (Water Survey of Canada). Vertical lines show the periods of the expedition legs.

entered the Beaufort Sea at that time. While the DOC concentration near the river mouth later in the year was still strongly associated with the Mackenzie runoff, the extent of the northward plume propagation appeared to vary independently. During the low discharge of the Mackenzie River, other processes such as ocean currents and winds likely controlled the propagation of the river plume in the Beaufort Sea (e.g. Carmack et al., 1989).

Overall, the applicability of SOCRS for this study benefited from exceptionally ice-free and relatively cloud-free conditions over large areas of the Beaufort Sea Shelf, as well as the early northward progression of the pack ice-edge in 2019. The use of SOCRS improved the extent of both spatial and temporal monitoring of river plume propagation and the distribution of DOC on the Beaufort Sea Shelf. Furthermore, SOCRS places in situ observations into a wider context, reveals transport pathways and indicates the speed of how rapid DOC concentrations in surface waters of Arctic shelves change.

4. Conclusion

In this study, we show that the Mackenzie Delta - Beaufort Sea region is characterized by a strong seasonal variability of the Mackenzie River plume propagation and the associated distribution of terrigenous DOC. We use collected in situ data to 1) evaluate and 2) improve the performance of SOCRS. Furthermore, this study demonstrates that SOCRS is a powerful tool to expand in situ observations and to improve our knowledge about distribution and transport of DOC. This is especially relevant in Arctic regions where in situ data are limited in spatial and temporal coverage partly due to significant logistical efforts.

Our results show that assessing the performance of atmospheric corrections in near-shore Arctic coastal waters remains challenging. This is on the one hand due to lack of valid match-up data related to clouds and ice, and on the other hand due to difficulties in obtaining accurate in situ ground truth data in highly turbid and/or absorbing waters as in this study.

In the coastal waters of the Beaufort Sea, the best (of three) performing atmospheric correction to retrieve $R_{rs}(\lambda)$ from Sentinel 3 OLCI imagery has mean bias of 9.25%. In combination with the best (of two) performing CDOM retrieval algorithm and our new DOC-CDOM relationship that is valid across river, coastal and marine waters, we show that SOCRS can be used to map DOC concentrations across the fluvial-marine transition zone over the Beaufort Sea Shelf with an accuracy of 20.5% (mean percentage error). With the new DOC-CDOM relationship, this study closes a critical gap by establishing a robust relationship between DOC and CDOM from river, coastal and offshore waters (0.0197

$m^{-1} < a_{CDOM}(443) < 2.612\ m^{-1}$, and 0.593 mg L^{-1} < DOC <7.12 mg L^{-1}), which is required for the retrieval of DOC concentration with SOCRS.

Currently, SOCRS is mostly limited to quantifying DOC. To examine the quality of DOC (e.g. degradational state and bioavailability) or sources of DOC (e.g. old permafrost-originating carbon vs. young vascular plant carbon), continuous field observations are necessary.

To evaluate the performance of SOCRS in other river-influenced Arctic seas and to identify potential regionally varying uncertainties of remotely-sensed DOC concentrations, extensive in situ data collections of radiometric and biogeochemical data from these regions are needed. Continuous in situ data collection and improvements in AC algorithms and CDOM and DOC retrieval will be necessary for an accurate estimation of carbon fluxes from land to the Arctic Ocean on a pan-Arctic scale. The projected decrease in sea ice extent and shortening of the ice-covered period will further increase the applicability of SOCRS in the Arctic. Future work on exploiting existing satellite data from the past ~20 years can reveal potential trends in fluxes of DOC associated with ongoing climate change in the Arctic.

Funding

This research has been supported by the EU Horizon 2020 programme (Nunataryuk, grant no. 773421), the Network of Centres of Excellence of Canada ArcticNet (P66-Nunataryuk), JAXA GCOM-C (Contract number: 19RT000542 and 20RT000350), NASA ROSES projects (Award number: 210319602), Québec-Océan, the Aurora Research Institute, and Fisheries and Oceans Canada through the Arctic Science Fund Research program. Furthermore, this research was supported by the Sentinel North program of Université Laval, made possible, in part, thanks to funding from the Canada First Research Excellence Fund.

Bennet Juhls (BJ) was supported by the Geo.X, the Research Network for Geosciences in Berlin and Potsdam (grant no. SO_087_GeoX), a Sentinel North mobility grant for a research stay in Quebec City (Université Laval). BJ was funded by the European Space Agency (ESA) as part of the Climate Change Initiative (CCI) fellowship (ESA ESRIN/Contract No. 4000l3376l/2l/I-NB).

I acknowledge support by the Open Access Publication Funds of Alfred-Wegener-Institut Helmholtz Zentrum für Polar- und Meeresforschung.

Credit author statement

B. Juhls and A. Matsuoka conceptualized the manuscript. B. Juhls conducted most processing, analysis, and lead the writing of the manuscript. A. Matsuoka, M. Lizotte and G. Bécu, P.P. Overduin, J. El Kassar, E. Devred, D. Doxaran, J. Ferland, M. H. Forget, A. Hilborn, M. Hieronymi, E. Leymarie, J. Maury, L. Oziel, L. Tisserand, M. Babin participated in writing the manuscript. J. El Kassar and M. Hieronymi participated in processing satellite data. B. Juhls, A. Matsuoka, M. Lizotte and G. Bécu, E. Devred, D. Doxaran, J. Ferland, A. Hilborn, E. Leymarie, J. Maury, L. Oziel, L. Tisserand conducted field work and lab analysis together with local field assistants D. O. J. Anikina and M. Dillon.

Declaration of Competing Interest

The authors declare that they have no known competing financial interests or personal relationships that could have appeared to influence the work reported in this paper.

Data availability

All in situ data are provided on PANGAEA archive for public access (https://doi.org/10.1594/PANGAEA.937587)

Acknowledgements

This project was conducted under the scientific coordination of the CNRS and Université Laval, International Research Laboratory Takuvik (IRL3376). We thank all participants of the expeditions and persons involved in the logistical support, including M. Béguin, T. Bossé-Demers, C. Guilmette, A. Laberge-Carignan and S. Antonova.

This project was made possible through the tremendous support of the hunters and trappers committees, the hamlet and town councils, the community corporations, as well as several members of the communities of Aklavik, Inuvik and Tuktoyaktuk. A special thanks goes out to our local research assistants: Raymond Ettagiak, Thomas Gordon and Sammy Gruben Jr.

We want to express our gratitude to Dustin Whalen (Natural Resources Canada), and Dr. Lisa Bröder (ETH, Zurich), for analytical and logistical support prior to and during field work. Further, we would like to thank Gaëlle Mevel for data collection and processing. Further, we thank Michael Angelopolous and Sofia Antonova for proof reading of this manuscript and Dr. Frederieke Miesner for valuable advice regarding statistical analysis.

Appendix

Flags used for different atmospheric corrections

Appendix Table 1
List of flags that were used to mask invalid pixel for satellite data extraction.

AC	Flags used
WFR	**Pixels excluded that were flagged with:** WQSF_lsb_LAND WQSF_lsb_CLOUD_AMBIGUOUS WQSF_lsb_CLOUD_MARGIN WQSF_lsb_SNOW_ICE WQSF_lsb_AC_FAIL WQSF_lsb_HISOLZEN WQSF_lsb_LOWRW WQSF_msb_ANNOT_TAU06
C2RCC	**Pixels excluded that were flagged with:** quality_flags_bright

(*continued on next page*)

Appendix Table 1 (*continued*)

AC	Flags used
Polymer	quality_flags_land quality_flags_invalid **Only pixels included that were flagged with:** 1024 (Case 2) 0 (no flag).

Number of observations for transect time series (Fig. 12)

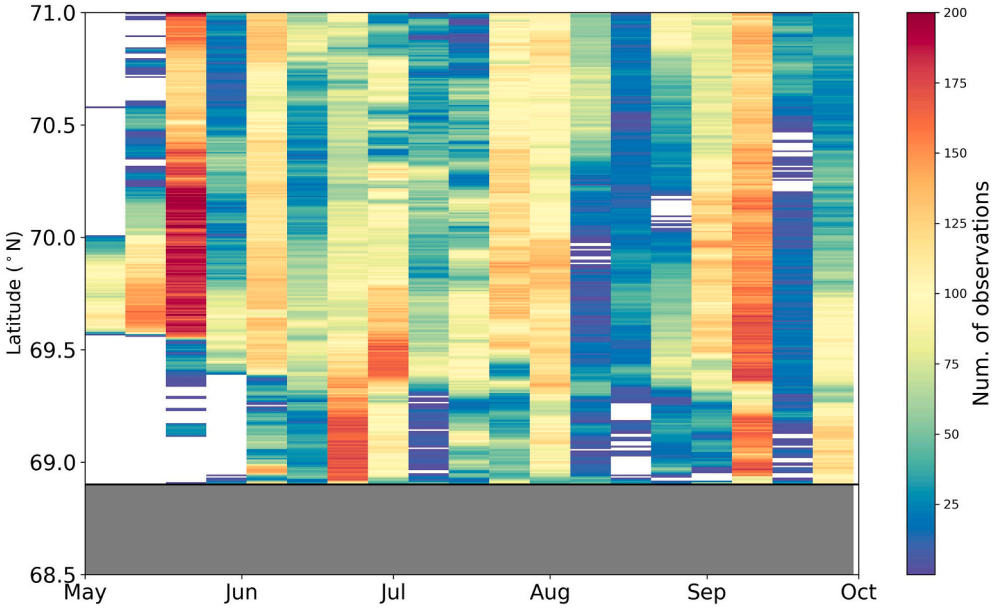

Appendix Fig. 1. Number of observations (sum of 9 pixel transect width) for each grid point of the extracted transect along 136.4°W.

Shading correction estimated by Monte Carlo

The physical dimensions of the C-OPS ICEPro (Appendix Fig. 2) were accurately transcribed in the Monte-Carlo modelling.

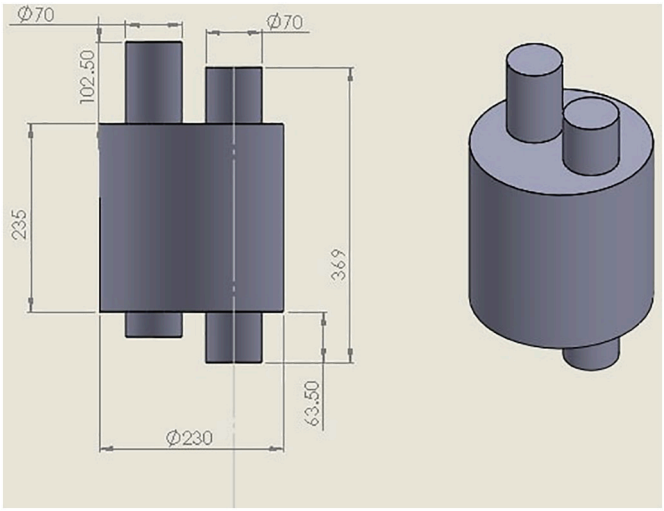

Appendix Fig. 2. Geometry used to simulate the C-OPS IcePro. The sensor is placed at a depth of 0.5 m.

The radiance sensor has an angular aperture of 3°. >80 virtual samples were simulated with absorption coefficients ranging from 0.1 to 12.5 m^{-1} and scattering coefficients ranging from 0.1 to 100 m^{-1}. Two particulate phase functions (Fournier-Forand) were used with backscattering ratios of 1.83 (from (Petzold et al., 1972) and 4% (selected value from measurements in similarly particle-loaded waters; McKee et al., 2009). Sky is assumed to be black (dominated by direct sunlight). The shading, i.e., the error on the measured $L_u(\lambda)$ signal due to self-shading induced by the C-OPS IcePro

estimated by Monte-Carlo, can be estimated from the quantity $x(\lambda) = a(\lambda) + b_b(\lambda)$ (Appendix Fig. 3).

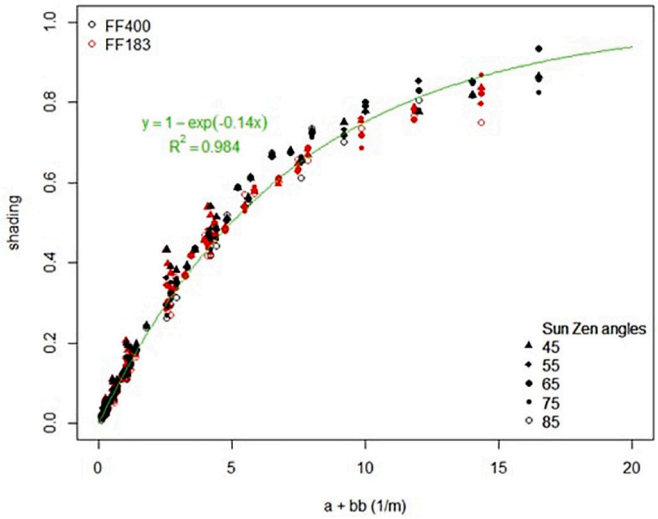

Appendix Fig. 3. Self shading induced by the IcePro estimated from Monte Carlo simulations in function of the quantity $a(\lambda) + b_b(\lambda)$ for various solar zenith angles from 45 to 85 deg. In black simulations are done with a back-scattering ratio of 4% and in red with 1.83%.

As it was not measured in the field, b_b was estimated from the measured absorption coefficient based on the Malina dataset (Doxaran et al., 2012). From this dataset, considering measurements carried out in the Mackenzie delta, the total scattering coefficient at 555 nm b(555) can be expressed as:

$$b(555) = 14.267 * a(555) + 0.8667, (n = 37)$$

Applied to this data set, $b(\lambda)$ was calculated as above for the 555 nm reference wavelength. It was assumed that the water contribution to light scattering was negligible compared to the contribution of suspended particles. For other wavelengths, we applied the following equation:

$$b(\lambda) = b(555) * \frac{\lambda}{555}^{-0.5},$$

where 0.5 is the mean spectral slope of the particulate scattering coefficient (Babin et al., 2003a). Then, b_b was estimated as $b_b = 0.04 * b$, where 0.04 is the backscattering ratio of 4%, assuming the water contribution to be negligible compared to the particulate contribution.

Performance of AC algorithms for all wavelengths

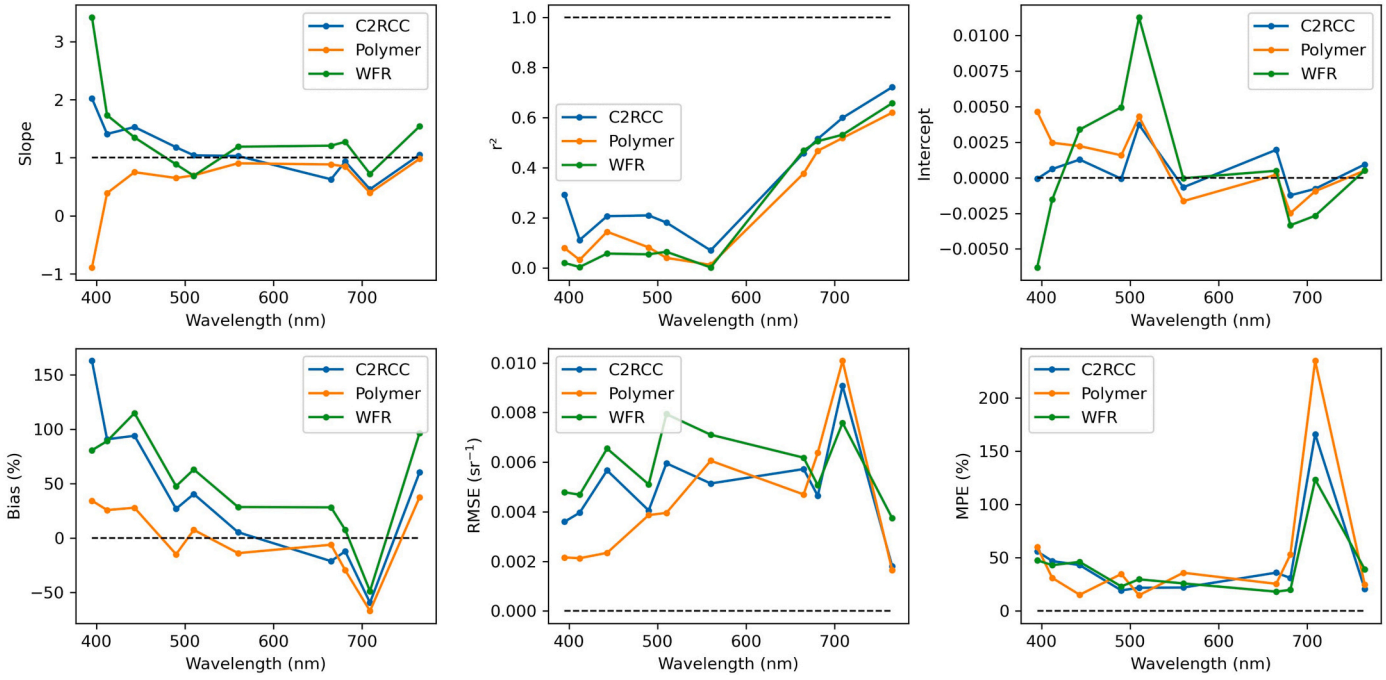

Appendix Fig. 4. Statistical performance of AC algorithms as a function of the S-3 bands.

Appendix Table 2
Statistics of AC algorithm performance for each wavelength.

	WFR												
λ (nm)	400	412	443	490	510	560	665	681	709	754	779	865	Mean
N	37	43	46	47	47	47	47	47	47	47	47	46	45.667
Slope	3.417	1.733	1.349	0.885	0.688	1.189	1.207	1.273	0.721	1.54	0.889	0.407	1.275
Intercept	−0.006	−0.002	0.003	0.005	0.011	−3.645	0.001	−0.003	−0.002	0.001	−0.001	−0.001	0.001
R^2	0.019	0.003	0.057	0.054	0.064	0.002	0.469	0.506	0.531	0.657	0.634	0.075	0.256
MPE (%)	47.555	42.948	46.007	22.996	29.652	25.829	18.075	19.8	123.283	39.157	36.232	168.107	51.637
RMSE (m^{-1})	0.005	0.005	0.007	0.005	0.008	0.007	0.006	0.005	0.008	0.004	0.002	0.002	0.005
Bias (%)	80.647	89.01	114.71	47.654	63.015	28.532	28.232	7.637	−48.604	96.432	−5.083	−11.584	40.883
	C2RCC												
N	48	54	58	59	59	59	59	59	59	59			57.300
Slope	2.019	1.409	1.528	1.18	1.041	1.029	0.628	0.933	0.457	1.051			1.128
Intercept	−7.734	0.001	0.001	−7.019	0.004	−0.001	0.002	−0.001	−0.001	0.001			0.001
R^2	0.292	0.111	0.206	0.209	0.181	0.069	0.458		0.599	0.721			0.34
MPE (%)	55.848	46.788	43.001	19.265	21.703	21.939	35.902	30.836	165.865	20.552			46.17
RMSE (m^{-1})	0.004	0.004	0.006	0.004	0.006	0.005	0.006	0.005	0.009	0.002			0.005
Bias (%)	162.649	90.708	93.928	26.878	40.464	5.398	−21.123	−12.115	−59.217	60.351			38.782
	Polymer												
N	51	57	60	61	61	61	61	61	61	61	61	60	59.667
Slope	−0.89	0.389	0.751	0.65	0.696	0.904	0.884	0.849	0.395	0.979	0.475	−0.54	0.462
Intercept	0.005	0.002	0.002	0.002	0.004	−0.002	0.001	−0.003	−0.001	0.001	0.001	0.002	0.001
R^2	0.079	0.032	0.144	0.082	0.04	0.012	0.377	0.467	0.519	0.62	0.603	0.035	0.251
MPE (%)	59.966	31.005	15.162	34.656	14.744	35.823	25.408	52.932	234.617	24.848	92.839	61.88	56.99
RMSE (m^{-1})	0.002	0.002	0.002	0.004	0.004	0.006	0.005	0.006	0.01	0.002	0.003	0.002	0.004
Bias (%)	34.335	25.758	27.867	−14.863	7.544	−13.772	−6.071	−29.399	−66.879	37.499	−28.177	61.003	2.908

References

Amon, R.M.W., Rinehart, A.J., Duan, S., Louchouarn, P., Prokushkin, A., Guggenberger, G., Bauch, D., Stedmon, C., Raymond, P.A., Holmes, R.M., McClelland, J.W., Peterson, B.J., Walker, S.A., Zhulidov, A.V., 2012. Dissolved organic matter sources in large Arctic rivers. Geochim. Cosmochim. Acta 94, 217–237. https://doi.org/10.1016/J.GCA.2012.07.015.

Antoine, D., Hooker, S.B., Bélanger, S., Matsuoka, A., Babin, M., 2013. Apparent optical properties of the Canadian Beaufort Sea – part 1: observational overview and water column relationships. Biogeosciences 10, 4493–4509. https://doi.org/10.5194/bg-10-4493-2013.

Babin, M., Arrigo, K., Bélanger, S., Forget, M.-H., Frouin, R., Hill, V., Hirawake, T., Matsuoka, A., Mitchell, B.G., Perovich, D., Reynolds, R.A., Stamnes, K., Wang, M., 2015. Ocean colour remote sensing in polar seas. International Ocean Colour Coordinating Group, Report Series No. 16, Dartmouth, Canada.

Babin, M., Morel, A., Fournier-Sicre, V., Fell, F., Stramski, D., 2003a. Light scattering properties of marine particles in coastal and open ocean waters asrelated to the particle mass concentration. Limnol. Oceanogr. 48, 843–859. https://doi.org/10.4319/LO.2003.48.2.0843.

Babin, M., Stramski, D., Ferrari, G.M., Claustre, H., Bricaud, A., Obolensky, G., Hoepffner, N., 2003b. Variations in the light absorption coefficients of phytoplankton, nonalgal particles, and dissolved organic matter in coastal waters around Europe. J. Geophys. Res. 108, 3211. https://doi.org/10.1029/2001JC000882.

Bailey, S.W., Werdell, P.J., 2006. A multi-sensor approach for the on-orbit validation of ocean color satellite data products. https://doi.org/10.1016/j.rse.2006.01.015.

Bélanger, S., Babin, M., Larouche, P., 2008. An empirical ocean color algorithm for estimating the contribution of chromophoric dissolved organic matter to total light absorption in optically complex waters. J. Geophys. Res. Ocean. 113 https://doi.org/10.1029/2007JC004436.

Bélanger, S., Carrascal-Leal, C., Jaegler, T., Larouche, P., Galbraith, P., 2017. Assessment of radiometric data from a buoy in the st. Lawrence estuary. J. Atmos. Ocean. Technol. 34, 877–896. https://doi.org/10.1175/JTECH-D-16-0176.1.

Belz, M., Dress, P., Sukhitskiy, A., Liu, S., 1999. Linearity and effective optical pathlength of liquid waveguide capillary cells. Intern. Stand. Calibration Archit. Chem. Sensors 3856, 271–281. https://doi.org/10.1117/12.371300.

Bertin, C., Matsuoka, A., Mangin, A., Babin, M., Le Fouest, V., 2022. Merging satellite and in situ data to assess the flux of terrestrial dissolved organic carbon from the Mackenzie river to the coastal beaufort sea. Front. Earth Sci. 10, 66. https://doi.org/10.3389/FEART.2022.694062/BIBTEX.

Carmack, E.C., Macdonald, R.W., Papadakis, J.E., 1989. Water mass structure and boundaries in the Mackenzie shelf estuary. J. Geophys. Res. 94, 18043. https://doi.org/10.1029/JC094IC12P18043.

Cooper, L.W., Mcclelland, J.W., Holmes, R.M., Raymond, P.A., Gibson, J.J., Guay, C.K., Peterson, B.J., 2008. Flow-weighted values of runoff tracers (d 18 O, DOC, Ba, alkalinity) from the six largest Arctic rivers. https://doi.org/10.1029/2008GL035007.

Doerffer, R., Schiller, H., 2007. The MERIS case 2 water algorithm. Int. J. Remote Sens. 28, 517–535. https://doi.org/10.1080/01431160600821127.

Doxaran, D., Ehn, J., Bélanger, S., Matsuoka, A., Hooker, S., Babin, M., 2012. Optical characterisation of suspended particles in the Mackenzie River plume (Canadian Arctic Ocean) and implications for ocean colour remote sensing. Biogeosciences 9, 3213–3229. https://doi.org/10.5194/bg-9-3213-2012.

Ehn, J.K., Reynolds, R.A., Stramski, D., Doxaran, D., Lansard, B., Babin, M., 2019. Patterns of suspended particulate matter across the continental margin in the Canadian Beaufort Sea during summer. Biogeosciences 16, 1583–1605. https://doi.org/10.5194/bg-16-1583-2019.

Emmerton, C.A., Lesack, L.F.W., Vincent, W.F., 2008. Mackenzie River nutrient delivery to the Arctic Ocean and effects of the Mackenzie Delta during open water conditions. Glob. Biogeochem. Cycles 22. https://doi.org/10.1029/2006GB002856.

Fichot, C.G., Kaiser, K., Hooker, S.B., Amon, R.M.W., Babin, M., Bélanger, S., Walker, S. A., Benner, R., 2013. Pan-Arctic distributions of continental runoff in the Arctic Ocean. Sci. Rep. 3, 1053. https://doi.org/10.1038/srep01053.

Forest, A., Coupel, P., Else, B., Nahavandian, S., Lansard, B., Raimbault, P., Papakyriakou, T., Gratton, Y., Fortier, L., Tremblay, J.É., Babin, M., 2014. Synoptic evaluation of carbon cycling in the Beaufort Sea during summer: contrasting river inputs, ecosystem metabolism and air-sea CO2 fluxes. Biogeosciences 11, 2827–2856. https://doi.org/10.5194/bg-11-2827-2014.

Frey, K.E., McClelland, J.W., 2009. Impacts of permafrost degradation on arctic river biogeochemistry. Hydrol. Process. https://doi.org/10.1002/hyp.7196.

Frey, K.E., Smith, L.C., 2005. Amplified carbon release from vast west siberian peatlands by 2100. Geophys. Res. Lett. 32, L09401. https://doi.org/10.1029/2004GL022025.

Gerbi, G.P., Boss, E., Jeremy Werdell, P., Proctor, C.W., Haëntjens, N., Lewis, M.R., Brown, K., Sorrentino, D., Zaneveld, J.R.V., Barnard, A.H., Koegler, J., Fargher, H., DeDonato, M., Wallace, W., 2016. Validation of ocean color remote sensing reflectance using autonomous floats. J. Atmos. Ocean. Technol. 33, 2331–2352. https://doi.org/10.1175/JTECH-D-16-0067.1.

Gonçalves-Araujo, R., Stedmon, C.A., Heim, B., Dubinenkov, I., Kraberg, A., Moiseev, D., Bracher, A., 2015. From fresh to marine waters: characterization and fate of dissolved organic matter in the Lena river delta region. Siberia. Front. Mar. Sci. 2, 108. https://doi.org/10.3389/fmars.2015.00108.

Gordon, H.R., Ding, K., 1992. Self-shading of in-water optical instruments. Limnol. Oceanogr. 37, 491–500.

Gossn, J., Ruddick, K., Dogliotti, A., 2019. Atmospheric correction of OLCI imagery over extremely turbid waters based on the red, NIR and 1016 nm bands and a new baseline residual technique. Remote Sens. 11, 220. https://doi.org/10.3390/rs11030220.

Granskog, M.A., Macdonald, R.W., Kuzyk, Z.Z.A., Senneville, S., Mundy, C.-J., Barber, D. G., Stern, G.A., Saucier, F., 2009. Coastal conduit in southwestern Hudson Bay (Canada) in summer: rapid transit of freshwater and significant loss of colored dissolved organic matter. J. Geophys. Res. 114 https://doi.org/10.1029/2009jc005270.

Hieronymi, M., 2019. Spectral band adaptation of ocean color sensors for applicability of the multi-water biogeo-optical algorithm ONNS. Opt. Express 27, A707. https://doi.org/10.1364/OE.27.00A707.

Hieronymi, M., Müller, D., Doerffer, R., 2017. The OLCI neural network swarm (ONNS): a bio-geo-optical algorithm for open ocean and coastal waters. Front. Mar. Sci. 4, 140. https://doi.org/10.3389/fmars.2017.00140.

Holmes, R.M., Coe, M.T., Fiske, G.J., Gurtovaya, T., McClelland, J.W., Shiklomanov, A.I., Spencer, R.G.M., Tank, S.E., Zhulidov, A.V., 2012a. Climate change impacts on the hydrology and biogeochemistry of arctic rivers. In: Climatic Change and Global Warming of Inland Waters. John Wiley & Sons Ltd, Chichester, UK, pp. 1–26. https://doi.org/10.1002/9781118470596.ch1.

Holmes, R.M., McClelland, J.W., Peterson, B.J., Tank, S.E., Bulygina, E., Eglinton, T.I., Gordeev, V.V., Gurtovaya, T.Y., Raymond, P.A., Repeta, D.J., Staples, R., Striegl, R. G., Zhulidov, A.V., Zimov, S.A., 2012b. Seasonal and annual fluxes of nutrients and organic matter from large rivers to the Arctic Ocean and surrounding seas. Estuar. Coasts 35, 369–382. https://doi.org/10.1007/s12237-011-9386-6.

Hooker, S.B., Morrow, J.H., Matsuoka, A., 2013. Apparent optical properties of the Canadian Beaufort Sea - part 2: the 1% and 1 cm perspective in deriving and validating AOP data products. Biogeosciences 10, 4511–4527. https://doi.org/10.5194/bg-10-4511-2013.

IOCCG, 2010. Atmospheric Correction for Remotely-Sensed Ocean-Colour Products. Dartmouth, NS, Canada (Reports of the International Ocean-Colour Coordinating Group, No. 10).

Juhls, B., Overduin, P.P., Hölemann, J., Hieronymi, M., Matsuoka, A., Heim, B., Fischer, J., 2019. Dissolved organic matter at the fluvial-marine transition in the Laptev Sea using in situ data and ocean colour remote sensing. Biogeosciences 16. https://doi.org/10.5194/bg-16-2693-2019.

Juhls, B., Stedmon, C.A., Morgenstern, A., Meyer, H., Hölemann, J., Heim, B., Povazhnyi, V., Overduin, P.P., 2020. Identifying drivers of seasonality in Lena River biogeochemistry and dissolved organic matter fluxes. Front. Environ. Sci. 8, 53. https://doi.org/10.3389/fenvs.2020.00053.

Lasareva, E.V., Parfenova, A.M., Romankevich, E.A., Lobus, N.V., Drozdova, A.N., 2019. Organic matter and mineral interactions modulate flocculation across Arctic River mixing zones. J. Geophys. Res. Biogeosciences 124, 1651–1664. https://doi.org/10.1029/2019JG005026.

Le Fouest, V., Babin, M., Tremblay, J.-É., 2013. The fate of riverine nutrients on Arctic shelves. Biogeosciences 10, 3661–3677. https://doi.org/10.5194/bg-10-3661-2013.

Lefering, I., Röttgers, R., Utschig, C., McKee, D., 2017. Uncertainty budgets for liquid waveguide CDOM absorption measurements. Appl. Opt. 56, 6357. https://doi.org/10.1364/ao.56.006357.

Leymarie, E., Doxaran, D., Babin, M., 2010. Uncertainties associated to measurements of inherent optical properties in natural waters. Appl. Opt. 49, 5415–5436. https://doi.org/10.1364/AO.49.005415.

Leymarie, E., Penkerc'h, C., Vellucci, V., Lerebourg, C., Antoine, D., Boss, E., Lewis, M.R., D'Ortenzio, F., Claustre, H., 2018. ProVal: a new autonomous profiling float for high quality radiometric measurements. Front. Mar. Sci. 5, 437. https://doi.org/10.3389/fmars.2018.00437.

Lizotte, M., Juhls, B., Matsuoka, A., Massicotte, P., Mével, G., Obie, D., Anikina, J., Antonova, S., Bécu, G., Béguin, M., Bélanger, S., Bossé-Demers, T., Bröder, L., Bruyant, F., Chaillou, G., Comte, J., Couture, R.-M., Devred, E., Deslongchamps, G., Dezutter, T., Dillon, M., Doxaran, D., Flamand, A., Fell, F., Ferland, J., Forget, M.-H., Fritz, M., Gordon, T.J., Guilmette, C., Hilborn, A., Hussherr, R., Irish, C., Joux, F., Kipp, L., Laberge-Carignan, A., Lantuit, H., Leymarie, E., Mannino, A., Maury, J., Overduin, P., Oziel, L., Stedmon, C., Thomas, C., Tisserand, L., Tremblay, J.-É., Vonk, J., Whalen, D., Babin, M., 2022. Nunataryuk field campaigns: understanding the origin and fate of terrestrial organic matter in the coastal waters of the Mackenzie delta region. Earth Syst. Sci. Data Discuss. https://doi.org/10.5194/essd-2022-163 [preprint] in review.

Macdonald, R.W., Paton, D.W., Carmack, E.C., Omstedt, A., 1995. The freshwater budget and under-ice spreading of Mackenzie river water in the Canadian beaufort sea based on salinity and 18O/16O measurements in water and ice. J. Geophys. Res. Ocean. 100, 895–919. https://doi.org/10.1029/94JC02700.

Mann, P.J., Davydova, A., Zimov, N., Spencer, R.G.M., Davydov, S., Bulygina, E., Zimov, S., Holmes, R.M., 2012. Controls on the composition and lability of dissolved organic matter in Siberia's Kolyma River basin. J. Geophys. Res. Biogeosciences 117. https://doi.org/10.1029/2011JG001798.

Mann, P.J., Spencer, R.G.M., Hernes, P.J., Six, J., Aiken, G.R., Tank, S.E., McClelland, J. W., Butler, K.D., Dyda, R.Y., Holmes, R.M., 2016. Pan-Arctic trends in terrestrial dissolved organic matter from optical measurements. Front. Earth Sci. 4, 25. https://doi.org/10.3389/feart.2016.00025.

Mannino, A., Russ, M.E., Hooker, S.B., 2008. Algorithm development and validation for satellite-derived distributions of DOC and CDOM in the U.S. Middle Atlantic Bight. J. Geophys. Res. Ocean. 113 https://doi.org/10.1029/2007JC004493.

Maritorena, S., Siegel, D.A., Peterson, A.R., 2002. Optimization of a semianalytical ocean color model for global-scale applications. Appl. Opt. 41, 2705. https://doi.org/10.1364/AO.41.002705.

Mannino, A., Novak, M.G., Nelson, N.B., Belz, M., Berthon, J.F., Blough, N.V., Boss, E., Bricaud, A., Chavez, J., Del Castillo, C., Del Vecchio, R., D'Sa, E.J., Freeman, S., Matsuoka, A., Miller, R.L., Neeley, A.R., Roettgers, R., Tzortziou, M., Werdell, P.J., Mannino, A. and Novak, M. G. (eds.), 2019. Measurement protocol of absorption by chromophoric dissolved organic matter (CDOM) and other dissolved materials, In Inherent Optical Property Measurements and Protocols: Absorption Coefficient. IOCCG Ocean Optics and Biogeochemistry Protocols for Satellite Ocean Colour Sensor Validation. (Dartmouth, NS, Canada.).

Massicotte, P., Amon, R., Antoine, D., Archambault, P., Balzano, S., Bélanger, S., Benner, R., Boeuf, D., Bricaud, A., Bruyant, F., Chaillou, G., Chami, M., Charrière, B., Chen, J., Claustre, H., Coupel, P., Delsaut, N., Doxaran, D., Ehn, J., Fichot, C., Forget, M.-H., Fu, P., Gagnon, J., Garcia, N., Ghiglione, J.-F., Gorsky, G., Gosselin, M., Gourvil, P., Gratton, Y., Guillot, P., Heipieper, H.J., Heussner, S., Hooker, S.B., Huot, Y., Jeanthon, C., Jeffrey, W., Joux, F., Kawamura, K., Lansard, B., Leymarie, E., Link, H., Lovejoy, C., Marec, C., Marie, D., Martin, J., Massé, G., Matsuoka, A., Mckague, V., Mignot, A., Miller, W.L., Miquel, J.-C., Mucci, A., Ono, K., Ortega-Retuerta, E., Panagiotopoulos, C., Papakyriakou, T., Picheral, M., Piepenburg, D., Prieur, L., Raimbault, P., Ras, J., Reynolds, R.A., Rochon, A., Rontani, J.-F., Schmechtig, C., Schmidt, S., Sempéré, R., Shen, Y., Song, G., Stramski, D., Stroud, D., Tachibana, E., Thirouard, A., Tolosa, I., Tremblay, J.-É., Vaïtilingom, M., Vaulot, D., Vaultier, F., Volkman, J.K., Vonk, J.E., Xie, H., Zheng, G., Babin, M., 2020. Earth System Science Data Discussions Earth System Science Data Discussions. https://doi.org/10.5194/essd-2020-252.

Massicotte, P., Asmala, E., Stedmon, C., Markager, S., 2017. Global distribution of dissolved organic matter along the aquatic continuum: across rivers, lakes and oceans. Sci. Total Environ. 609, 180–191. https://doi.org/10.1016/J.SCITOTENV.2017.07.076.

Matsuoka, A., Babin, M., Devred, E.C., 2016. A new algorithm for discriminating water sources from space: a case study for the southern Beaufort Sea using MODIS Ocean color and SMOS salinity data. Remote Sens. Environ. 184, 124–138. https://doi.org/10.1016/J.RSE.2016.05.006.

Matsuoka, A., Boss, E., Babin, M., Karp-Boss, L., Hafez, M., Chekalyuk, A., Proctor, C.W., Werdell, P.J., Bricaud, A., 2017. Pan-Arctic optical characteristics of colored dissolved organic matter: tracing dissolved organic carbon in changing Arctic waters using satellite ocean color data. Remote Sens. Environ. 200, 89–101. https://doi.org/10.1016/J.RSE.2017.08.009.

Matsuoka, A., Bricaud, A., Benner, R., Para, J., Sempéré, R., Prieur, L., Bélanger, S., Babin, M., 2012. Tracing the transport of colored dissolved organic matter in water masses of the southern Beaufort Sea: relationship with hydrographic characteristics. Biogeosciences 9, 925–940. https://doi.org/10.5194/bg-9-925-2012.

Matsuoka, A., Campbell, J.W., Hooker, S.B., Steinmetz, François, Ogata, Kazunori, Hirata, T., Higa, H., Victor, Kuwahara, Isada, Tomonori, Suzuki, K., Hirawake, T., Ishizaka, J., Murakami, Hiroshi, 2021. Performance of JAXA's SGLI standard ocean color products for oceanic to coastal waters: chlorophyll a concentration and light absorption coefficients of colored dissolved organic matter. J. Oceanogr. 93, 1–22. https://doi.org/10.1007/S10872-021-00617-2, 2021.

Matsuoka, A., Hooker, S.B., Bricaud, A., Gentili, B., Babin, M., 2013. Estimating absorption coefficients of colored dissolved organic matter (CDOM) using a semi-analytical algorithm for southern Beaufort Sea waters: application to deriving concentrations of dissolved organic carbon from space. Biogeosciences 10, 917–927. https://doi.org/10.5194/bg-10-917-2013.

McClelland, J.W., Déry, S.J., Peterson, B.J., Holmes, R.M., Wood, E.F., 2006. A pan-arctic evaluation of changes in river discharge during the latter half of the 20th century. Geophys. Res. Lett. 33, L06715. https://doi.org/10.1029/2006GL025753.

McClelland, J.W., Holmes, R.M., Dunton, K.H., Macdonald, R.W., 2012. The Arctic Ocean estuary. Estuar. Coasts. https://doi.org/10.1007/s12237-010-9357-3.

McGuire, A.D., Anderson, L.G., Christensen, T.R., Scott, D., Laodong, G., Hayes, D.J., Martin, H., Lorenson, T.D., Macdonald, R.W., Nigel, R., 2009. Sensitivity of the carbon cycle in the arctic to climate change. Ecol. Monogr. https://doi.org/10.1890/08-2025.1.

McKee, D., Chami, M., Brown, I., Calzado, V.S., Doxaran, D., Cunningham, A., 2009. Role of measurement uncertainties in observed variability in the spectral backscattering ratio: a case study in mineral-rich coastal waters. Appl. Opt. 48 (24), 4663–4675. https://doi.org/10.1364/AO.48.004663, 48, 4663–4675.

Mobley, C.D., 1999. Estimation of the remote-sensing reflectance from above-surface measurements. Appl. Opt. 38, 7442. https://doi.org/10.1364/AO.38.007442.

Mograne, M., Jamet, C., Loisel, H., Vantrepotte, V., Mériaux, X., Cauvin, A., 2019. Evaluation of five atmospheric correction algorithms over french optically-complex waters for the sentinel-3A OLCI Ocean color sensor. Remote Sens. 11, 668. https://doi.org/10.3390/rs11060668.

Moore, G.F., Aiken, J., Lavender, S.J., 2010. The atmospheric correction of water colour and the quantitative retrieval of suspended particulate matter in case II waters: application to MERIS. Int. J. Remote Sens. 20, 1713–1733. https://doi.org/10.1080/014311699212434.

Morrow, J.H., Hooker, S.B., Booth, C.R., Bernhard, G., Lind, R.N., Brown, J.W., 2010. Advances in Measuring the Apparent Optical Properties (AOPs) of Optically Complex Waters.

Mulligan, R.P., Perrie, W., 2019. Circulation and structure of the Mackenzie River plume in the coastal Arctic Ocean. Cont. Shelf Res. 177, 59–68. https://doi.org/10.1016/J.CSR.2019.03.006.

Neeley, A.R., Mannino, A., Boss, E., D'sa, E.J., Freeman, S., Fry, E., Mueller, J.L., Pegau, S., Reynolds, R.A., Roesler, C., Rottgers, R., Stramski, D., Twardowski, M., Ronald, J., Zaneveld, V., 2018. IOCCG Protocol Series Ocean Optics & Biogeochemistry Protocols for Satellite Ocean Colour Sensor Validation Volume 1: Inherent Optical Property Measurements and Protocols: Absorption Coefficient (vl. O) Editors. https://doi.org/10.25607/OBP-119.

Obu, J., Westermann, S., Bartsch, A., Berdnikov, N., Christiansen, H.H., Dashtseren, A., Delaloye, R., Elberling, B., Etzelmüller, B., Kholodov, A., Khomutov, A., Kääb, A., Leibman, M.O., Lewkowicz, A.G., Panda, S.K., Romanovsky, V., Way, R.G., Westergaard-Nielsen, A., Wu, T., Yamkhin, J., Zou, D., 2019. Northern hemisphere permafrost map based on TTOP modelling for 2000–2016 at 1 km2 scale. Earth-Science Rev. https://doi.org/10.1016/j.earscirev.2019.04.023.

Osburn, C.L., Retamal, L., Vincent, W.F., 2009. Photoreactivity of chromophoric dissolved organic matter transported by the Mackenzie River to the Beaufort Sea. Mar. Chem. 115, 10–20. https://doi.org/10.1016/j.marchem.2009.05.003.

Peterson, B.J., 2002. Increasing River Discharge to the Arctic Ocean. Science 298, 2171–2173. https://doi.org/10.1126/science.1077445 (80-.).

Petzold, T.J., Duntley, S.Q., Nierenberg, W.A., 1972. Volume Scattering Functions for Selected Ocean Waters, 48, 4663–4675.

Pugach, S.P., Pipko, I.I., Shakhova, N.E., Shirshin, E.A., Perminova, I.V., Gustafsson, Ö., Bondur, V.G., Ruban, A.S., Semiletov, I.P., 2018. Dissolved organic matter and its

optical characteristics in the laptev and east siberian seas: spatial distribution and interannual variability. Ocean Sci. https://doi.org/10.5194/os-14-87-2018.

Raymond, P.A., McClelland, J.W., Holmes, R.M., Zhulidov, A.V., Mull, K., Peterson, B.J., Striegl, R.G., Aiken, G.R., Gurtovaya, T.Y., 2007. Flux and age of dissolved organic carbon exported to the Arctic Ocean: a carbon isotopic study of the five largest arctic rivers. Glob. Biogeochem. Cycles 21. https://doi.org/10.1029/2007GB002934.

Renosh, P.R., Doxaran, D., De Keukelaere, L., Gossn, J.I., 2020. Evaluation of atmospheric correction algorithms for sentinel-2-MSI and sentinel-3-OLCI in highly turbid estuarine waters. Remote Sens. 12, 1285. https://doi.org/10.3390/RS12081285.

Retamal, L., Bonilla, S., Vincent, W.F., 2008. Optical gradients and phytoplankton production in the Mackenzie River and the coastal Beaufort Sea. Polar Biol. 31, 363–379. https://doi.org/10.1007/s00300-007-0365-0.

Shen, Y., Fichot, C.G., Benner, R., 2012. Dissolved organic matter composition and bioavailability reflect ecosystem productivity in the Western Arctic Ocean. Biogeosciences 9, 4993–5005. https://doi.org/10.5194/bg-9-4993-2012.

Stedmon, C.A., Amon, R.M.W., Rinehart, A.J., Walker, S.A., 2011. The supply and characteristics of colored dissolved organic matter (CDOM) in the Arctic Ocean: pan Arctic trends and differences. Mar. Chem. 124, 108–118. https://doi.org/10.1016/J.MARCHEM.2010.12.007.

Steinmetz, F., Deschamps, P.-Y., Ramon, D., 2011. Atmospheric correction in presence of sun glint: application to MERIS. Opt. Express 19, 9783. https://doi.org/10.1364/oe.19.009783.

Tank, S.E., Striegl, R.G., McClelland, J.W., Kokelj, S.V., 2016. Multi-decadal increases in dissolved organic carbon and alkalinity flux from the Mackenzie drainage basin to the Arctic Ocean. Environ. Res. Lett. 11 https://doi.org/10.1088/1748-9326/11/5/054015.

Tilstone, G.H., Pardo, S., Simis, S.G.H., Qin, P., Selmes, N., Dessailly, D., Kwiatkowska, E., 2021, 14, 89. https://doi.org/10.3390/RS14010089.

Vallières, C., Retamal, L., Ramlal, P., Osburn, C.L., Vincent, W.F., 2008. Bacterial production and microbial food web structure in a large arctic river and the coastal Arctic Ocean. J. Mar. Syst. 74, 756–773. https://doi.org/10.1016/j.jmarsys.2007.12.002.

Vetrov, A.A., Romankevich, E.A., Vetrov, A.A., Romankevich, E.A., 2004. Horizontal carbon fluxes in the Land-Sea system. In: Carbon Cycle in the Russian Arctic Seas. Springer, Berlin Heidelberg, pp. 201–227. https://doi.org/10.1007/978-3-662-06208-1_5.

Yang, D., Shi, X., Marsh, P., 2015. Variability and extreme of Mackenzie River daily discharge during 1973–2011. Quat. Int. 380–381, 159–168. https://doi.org/10.1016/j.quaint.2014.09.023.

Zibordi, G., Voss, K.J., Johnson, B.C., Mueller, J.L., 2019. IOCCG Ocean optics and biogeochemistry protocols for satellite ocean colour sensor validation. IOCCG Protoc. Ser. 3 https://doi.org/10.25607/OBP-691.